A STUDY TOWARD LARGE-AREA LOW-DEFECT NANOSPHERE LITHOGRAPHY

BY

SARTAJ S. GREWAL

DISSERTATION

Submitted in partial fulfillment of the requirements
for the degree of Doctor of Philosophy in Electrical and Computer Engineering
in the Graduate College of the
University of Illinois Urbana-Champaign, 2021

Urbana, Illinois

Doctoral Committee:

Professor Joseph W. Lyding, Chair
Professor Catherine J. Murphy
Professor Xiuling Li
Associate Professor Qian Chen
Assistant Professor Kejie Fang

ABSTRACT

Surface-enhanced Raman spectroscopy (SERS) is a powerful label-free molecular characterization technique that detects ultra-low analyte concentrations. The critical requirement for the SERS enhancement effect is the presence of large magnitude electromagnetic fields existing between small-gap nanoparticle dimers. Considerable research effort is devoted to developing uniform and high enhancement response from SERS-based sensors. The achievement of this aim using uncomplicated and low-cost methods remains an active challenge nonetheless. Nanosphere lithography (NSL) leverages the benefits of a self-assembled nanosphere mask to deliver spontaneous high-density patterning of triangular nanoparticles. The use of a two-step shadow evaporation method with NSL masks creates programmable gap nanoparticle dimers. However, reliable control over the dimer gap requires further study of the mask properties.

This thesis aims to combine the shadow evaporation method with large-area single-crystalline nanosphere masks to create sub-10 nm gap nanoparticle dimer arrays. A novel dynamic self-assembly process for large-area quasi-single crystals of polymeric spheres is detailed. The addition of propylene glycol to the colloidal solution and low-velocity air and low-frequency acoustic external energy input unlocks the reliable fabrication of high-quality masks. The short-range and long-range defect density characterization identifies sphere polydispersity and evaporation-induced line defects as the primary causes of defect generation. Solvent treatment of the colloidal crystal reduces mean defect density by a factor of 5x with complete elimination of evaporation-induced line defects. The long-range orientation of the colloidal crystal is preferentially realigned to a single orientation using a hexagonal hydrophobic template. Nanoparticle arrays made from the improved masks demonstrate enhancement factors of 8.95×10^6 and uniformities below 12%.

To mom and dad

ACKNOWLEDGMENTS

First and foremost, I would like to thank my advisor Prof. Joe Lyding. It would have been impossible to undertake this ambitious project without Joe's constant support and guidance. As a part of the Lyding group, I have been able to grow in exponential ways and have worked alongside exceptional colleagues. I would like to thank all of the past and present Lyding group members for being an integral part of my graduate journey.

I would like to thank my doctoral committee comprising Prof. Joe Lyding, Prof. Catherine Murphy, Prof. Xiuling Li, Prof. Qian Chen, and Prof. Kejie Fang. The committee's feedback and suggestions were instrumental in shaping my research direction.

I would like to thank Dane Sievers for introducing me to the fun and collaborative ECEB Nanolab environment. I would like to thank my colleagues, Lukas Janavicius, Jamie Milota, Martin Evtimov, Daniel Vaz, Julian Michaels, Andrey Miranov, and Matthew Clawson for making this true. I have had the most fun and illuminating experiences working in the Nanolab. I am excited to see all the current and future technologies coming out of this collaborative space.

Lastly, I would like to thank all of the innumerable friends, colleagues, staff, and faculty that were an essential part of my life at the University of Illinois. I truly thank all of you. I would also like to thank my family for their unconditional love and support.

TABLE OF CONTENTS

CHAPTER 1

INTRODUCTION

1.1 Motivation

Raman spectroscopy is a label-free light spectroscopy technique that provides molecular identification of analytes by observing the vibrational, rotational, and other low-frequency modes [1]. The process starts with the excitation of analyte molecules to higher vibrational and rotational states by laser irradiation. The resultant relaxation to the ground state generates phonons and energy-shifted (lower energy) emitted photons. The energy shift between the source and the emitted photons relays sufficient information for precise characterization of the molecular structure. However, the Raman scattering process is an inelastic scattering process and, therefore, suffers from low intensities and low signal-to-noise ratios. The inelastically scattered light can be highly enhanced (orders of 6 to 14) by placing the analyte molecules close to metal nanoparticles or rough metal surfaces. This variant is aptly named surface-enhanced Raman spectroscopy (SERS).

Interaction between the laser radiation and the sub-diffraction length particles having negative real and small positive imaginary dielectric constants [2, 3] generate localized surface plasmon resonances (LSPRs). LSPRs are coherent conduction electron oscillations that produce intense electric fields on the metal surface. These electric fields are the dominant contributor to the overall SERS enhancement factor. LSPRs are dependent on the shape, size, spacing, orientation, and refractive indices of the nanoparticles and the environment [4]. Researchers have shown that low aspect ratio spherical particles demonstrate LSPR peaks in the green part of the visible electromagnetic spectrum with electric field enhancement around 10^4 [5]. Higher aspect ratio triangular particles demonstrate a red-shifted LSPR peak with electric field enhancement around 10^8. This peak shift is due to the free-

electron metal response at higher wavelengths and the lightning rod effect. As a result, the two-dimensional arrays of monomer particles demonstrate from 10^7 to 10^9 SERS enhancement levels [6]. Replacing monomer particles with dimer particles achieves an exponential increase in SERS enhancement levels approaching 10^{12} with a reduction in nanoparticle separations down to sub-10 nm [7, 8]. Thereby, substrate-based SERS sensors can detect single analyte molecules.

Currently, the widespread application of SERS as a clinical diagnostic tool is not hindered by an urgent need for high enhancement substrates [9, 10]. In fact, many examples have been presented of such substrates [7, 8, 11–28]. However, the deterministic patterning of defect-free and uniform response substrates is still an active area of research. This purpose needs to be undertaken using uncomplicated, low-cost, and novel processing methods and materials [29]. Single monolayer detection capabilities have been unlocked by fabrication of sub-10 nm gap nanoparticle dimers through chemical synthesis methods [30–33] and lithographic patterning using electron-beam lithography (EBL) [7, 8, 11]. However, chemically fabricated systems lack reproducibility and small surface areas of active plasmonic sites, and EBL suffers from high costs and low throughputs. The plasmon response of a nanoparticle dimer is highly sensitive to the variances of the interparticle gap [11, 12]. The resultant SERS response is also highly sensitive to the proximity of the molecular analyte to the hot spot in between the nanoparticles. Therefore, the target process should have the minimum feature variances associated with bottom-up processes and the high-density patterning capability of top-down processes.

1.2 Nanosphere Lithography

Nanosphere lithography (NSL) is a low-cost, materials general, inherently parallel, and high throughput bottom-up fabrication technique [4]. The characteristic feature of NSL is a self-assembled nanosphere monolayer shown in Figure 1.1a. The nanosphere monolayer is an inherently patterned mask for top-down processing techniques resulting in spontaneous large-area sub-diffraction limit lithography. The lithographic feature size is linked to the diameter of a single constituent nanosphere and can be varied from sub-50 nm

to 10 µm. Therefore, NSL offers a more cost-effective option compared to serial fabrication with electron beam lithography. NSL has been widely applied to make surface-enhanced Raman sensors [4, 22], metasurfaces [34–36], photovoltaics [37], resistive switching memory [38], transparent electrodes [39], light-emitting diode arrays [40], chemical sensors [41, 42], superhydrophobic surfaces [43] and lasers [44].

NSL is ideally suited for deterministic high-density patterning of SERS surfaces. The inverse pattern of the self-assembled colloidal mask is a hexagonally symmetric nanoparticle array shown in Figure 1.1b. The nanoparticle array is produced by evaporating a 30 nm gold layer on the nanosphere mask layer. The nanoparticles intrinsically possess an anisotropic triangular shape (Figure 1.1c), which demonstrates ultra-high plasmonic electric field enhancement [5]. The theoretical relations between the nanosphere diameter of 1 µm (D), the mean particle size (a) and the mean interparticle (tip to tip) distance (d_{ip}) are [4],

$$a = 1.5 \times (\sqrt{3} - 1 - \frac{1}{\sqrt{3}}) \times D = 232\ nm, \tag{1.1}$$

$$d_{ip} = \frac{D - 2 \times a}{\sqrt{3}} = 268\ nm. \tag{1.2}$$

The interparticle distances are much greater than the plasmon field propagation length of ∼15 nm [45]. Therefore, no near-field coupling is expected between the nanoparticles. The interparticle gap can be decoupled from the nanosphere diameter by producing two nanoparticle arrays displaced to each other in the substrate plane. This process is performed by simply varying the substrate and the metal source angle across two evaporation steps. The resultant technique is called angle-resolved nanosphere lithography (ARNSL). ARNSL can be used to produce nanogap, nanoverlap, or chained structures [4, 46]. Figure 1.1d shows an example of a nanogap array made by ARNSL. Small dimer gaps up to 4 nm can be produced with this technique [4, 47].

Bottom-up techniques like NSL are incredibly cost-effective at producing nanoscale objects. The number of nanoparticles fabricated for a 1 cm^2 of NSL mask area is calculated as follows. Assuming a unit cell of seven spheres

(radius r) shown in Figure 1.1e, the area of a unit cell hexagon (A) is

$$A = \frac{3 \times \sqrt{3}}{2} \times (2 \times r)^2 = 2.6 \times 10^{-8} \text{ cm}^2. \tag{1.3}$$

The number of interstitial sites (N) in a 1 cm^2 area is

$$N = 6 \times \text{Number of unit cells} = 6 \times \frac{1 \text{ cm}^2}{A} = 1.56 \times 10^9. \tag{1.4}$$

Therefore, NSL is capable of the spontaneous production of high-density arrays of plasmonic nanoparticles.

It is evident from Figure 1.1d that the uniformity of the small gap dimers produced from ARNSL is primarily dictated by the mask layer uniformity. Therefore, there is a need for reliable self-assembly of large-area low-defect single-crystalline colloidal masks. The colloidal mask layer can be fabricated through dip coating [48], spin coating [49, 50], convective assembly [51–53], Langmuir-Blodgett assembly [54] or air-water interfacial assembly [55–59]. There have also been several attempts at reducing colloidal crystal defect density. Individual grains have been reoriented into larger centimeter-scale grains with external energy sources of ultrasonics [54], acoustics [60] and gas flow [55, 58]. It has been shown that tuning the surface chemistry of the nanospheres with surfactants allows for more optimal loading [59] and a decrease in hydrophobic-hydrophobic interactions to allow easier reorientation [55,61]. Solvent annealing of the mask layer before deposition covalently bonds the neighboring nanospheres, thereby increasing the barrier to line defect generation [62]. Ring confinement has been used to achieve a smooth, defect-free, and precise transfer to the target substrate [56].

1.3 Proposed Approach and Thesis Structure

This thesis aims at reproducible fabrication of large-area uniform arrays of gold dimer particles with sub-10 nm gaps. The process starts with the fabrication of a large-area low-defect single-crystal colloidal mask layer. Two sequential evaporation steps of gold layers at distinct angles through the mask fabricates displaced particle arrays resulting in small gap dimers. The critical factors of the fabrication process are tested for a rigid hydrophilic sub-

strate (silicon) and a flexible hydrophobic substrate (polydimethylsiloxane), ensuring the universal applicability of the described method.

The remaining parts of the thesis are divided into three chapters. Chapter 2 introduces the traditional air-water interfacial self-assembly of a colloidal mask layer. The interplay between the attractive and the repulsive forces during self-assembly is detailed. It is realized that a conventional air-water interfacial process results in a polycrystalline close-packed monolayer of polymeric nanospheres. Standard atomic defects of vacancy defects, line defects, and grain boundaries are analogously found in the colloidal monolayer. Additional defect types of evaporation-induced line defects and nanosphere polydispersity are established. It is shown that the aggressive dewetting forces on a PDMS substrate cause the cracking of colloidal masks.

Chapter 3 introduces a simplified colloidal mask assembly process for large-area quasi-single crystals. An air-water interfacial assembly process is developed where the water layer and the nanosphere crystal are bound by the physical boundary of the silicon wafer. The convective evaporation of a high vapor pressure alcohol (isopropanol) transports the nanospheres to the air-water interface. Low vapor alcohol (propylene glycol) decreases the hydrophobic-hydrophobic interactions, which results in easy reorientation of the nanosphere aggregates into larger crystals. The reorientation is performed using low-velocity air currents and low-frequency acoustic vibrations. The colloidal mask defect density characterization using scanning electron microscopy (SEM) establishes the evaporation-induced line defects as a significant defect source. A solvent treatment process of the nanosphere crystal is applied to eliminate this defect type. Hence, defect densities are shown to improve by 5x as compared to non-treated crystals. The crystal twist is measured using laser diffraction. A strategy for fabricating large-area single crystals based on template enforcement is shown.

Chapter 4 studies the SERS sensors fabricated from the optimized colloidal masks developed in the Chapter 3. Physical vapor deposition of gold layers through the mask spontaneously creates sensor-scale arrays of gold nanoparticles. The size, shape, and spacing of the nanoparticles are characterized using SEM. The reflectance properties of the nanoparticle array for visible to near-infrared illumination are measured. The blue shift of the LSPR peak with an increase in the evaporated metal thickness is measured. The LSPR peak is optimally placed next to the 532 nm laser excitation wavelength by

increasing the silicon oxide thickness on the substrates. These optimized arrays demonstrate an enhancement factor (EF) of 8.95×10^6 for adsorbed adenine monolayers. The demonstrated EF compares well with literature for non-resonant molecules on monomer particles. A detailed study of the SERS spectra shows adsorption through the N7 and the amine side group sites. The role of the Raman cross-section of an analyte is studied by comparing SERS spectra from adenine and rhodamine 6G.

The alignment between the grain orientation and the substrate to the metal source orientation differentiates the nanoparticle arrays fabricated by ARNSL. The ability to controllably decrease the interparticle gap is demonstrated. Nanoparticle arrays fabricated on PDMS substrates are characterized using environmental SEM. The ability to tune interparticle gaps with substrate strain is shown.

Chapter 5 details the future work intended toward the thesis goal of reliable fabrication of sub-10 nm gap dimer particle arrays.

1.4 Figure

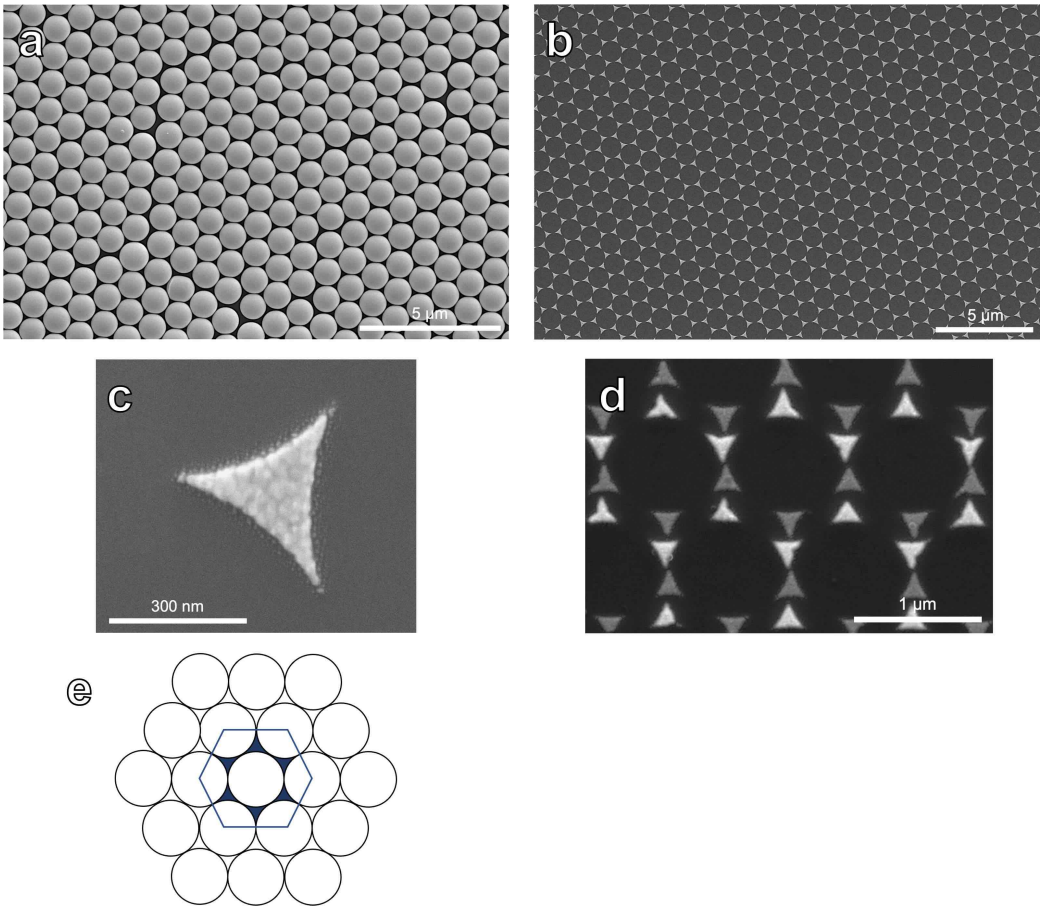

Figure 1.1: (a) Self-assembled colloidal mask, (b) Hexagonally symmetric nanoparticle array, (c) Morphology of a single triangular nanoparticle, (d) Nanoparticle array fabricated by two-step ARNSL at $\pm$ 15^o, (e) 2D hexagonal packing unit cell.

CHAPTER 2

COLLOIDAL MASK FABRICATION

2.1 Assembly Process

In a typical Langmuir-Blodgett trough, molecular layers are assembled on the air-water interface, and the physical properties are studied as a result of compression induced by barriers [63]. This approach has studied various molecules, including amphiphilic molecules, polymeric nanoparticles, metallic nanoparticles, lipid molecules, etc. For polymeric nanoparticles, the colloidal recipe comprising nanospheres and alcohols is applied to a flat air-water interface and allowed to form primary aggregates. The primary aggregates have a significant separation between them and are labeled as gas phase. Close packing is achieved by decreasing the available surface area by moving the barriers closer together. Assembly on hydrophilic substrates is completed by withdrawing the substrate from the bulk of the sub-phase (water) upwards and applying constant compression, thereby achieving a uniform deposition.

Close-packed colloidal crystals of hydrophobic polymeric particles have been a well-researched topic since the 1980s. It has been established that defect-free crystal lattices can be achieved by tuning the balance of attractive and repulsive forces dictated by the sphere surface properties. For the relevant diameters of 200 nm to 1 µm, the competing forces are the hydrophobic-hydrophobic interactions, surface tension forces, and electrostatic repulsion forces [55, 64, 65]. Commercially available nanosphere solutions contain a small amount of surfactant that adsorbs on the nanosphere surface and prevents aggregation. The nanosphere surface charge is the origin of the electrostatic repulsion between the spheres. Surface tension forces originating from solvent carriers (isopropanol or ethanol) in the colloidal solution are commonly employed to overcome this repulsion. Once the spheres approach each other, the hydrophobic-hydrophobic interactions enable close-packing.

Hydrophobic-hydrophobic interactions originate from the interaction of the nanosphere surface and the water molecules and are dictated by the wettability of the nanospheres [64, 66]. However, the hydrophobic-hydrophobic interactions need to be mediated to rearrange the crystal into a more defect-free close packing structure [64]. This concept will be explored in more detail in the next chapter.

The hexagonal close packed structure is the most thermodynamically stable packing structure for spherical nanospheres. Therefore, the Langmuir-Blodgett assembly process can be simplified with the optimal tuning of the attractive and repulsive forces. This simplified variation is the air-water interfacial assembly process. The key differences are simplifying the setup, and the mechanism to achieve close packing explained as follows. A typical setup for the air-water interfacial assembly process is shown in Figure 2.1a. The setup comprises an assembly trough filled with deionized water (DI), a submerged hydrophilic wafer, and an outlet to a syringe pump or a draining outlet. The assembly process has a fixed interface area dictated by the trough size. The colloidal solution comprises equal parts of 1 µm polystyrene nanosphere liquid and ethanol. The solution is slowly added to the interface by pipetting on a transfer silicon wafer and dipping the transfer wafer into the bulk of the sub-phase. Alternatively, a syringe is used to apply the colloidal solution directly to the air-water interface.

The resultant loose-packed nanosphere monolayer is shown in Figure 2.1b. Close hexagonal packing is achieved by pipetting 2-4 µl of 2% sodium dodecyl sulfate (SDS) solution directly onto the air-water interface. The generated surface tension forces overcomes the repulsion forces [57] to result in a polycrystalline film as shown in Figure 2.1c. It should be noted that larger interface areas will require higher sphere area density and larger surface tension forces to achieve compaction. The colorful diffracting part is a monolayer, while the small white parts are the multilayers. As the multilayer defects are a consequence of the loading process employing a transfer wafer, a more sophisticated method employing direct loading onto the air-water interface using a needle tip and control over the colloidal solution zeta potential can be employed [58, 59]. Finally, a syringe pump slowly removes DI from the trough, and the spheres gently assemble on the silicon substrate. The trough is angled at 5^{o} using a block to achieve a linear drying front. Figure 2.1d shows the silicon substrate after drying in air overnight. Centimeter-scale

coverage is achieved; however, the colloidal crystal tends to crack due to stress during the transfer process.

2.2 Defect Characterization

Large-area high-vacuum scanning electron microscopy (SEM) is employed to characterize the quality of the monolayer colloidal mask layer. Figure 2.2a shows a typical large-area SEM scan for a metal-coated mask layer. The lateral grain sizes range from 10 µm to above 100 µm with no correlation between adjacent grain sizes or grain orientations [67]. Crystal defects are shown in Figure 2.2b,c. These defects are labeled as vacancy defects, miscoordinated spheres, triplet defects, line defects and grain boundaries. Figure 2.2d shows the excellent hexagonal symmetry of the colloidal crystal and a defect of nanosphere polydispersity. The air-water interfacial assembly has shown compatibility from spheres with diameters ranging from 100 nm to 2 µm [57]. A colloidal crystal comprising of 500 nm diameter polystyrene spheres is shown in Figure 2.3. The equilateral height of the resultant nanoparticles is reduced by 50% compared to the nanoparticles fabricated from micron-sized colloidal masks.

2.3 Colloidal Mask Assembly on Soft Substrates

Sylgard 184 polydimethylsiloxane (PDMS) is widely used in stretchable sensors as it demonstrates high failure strains up to 160% [68], near-unity transmittance across the visible and near-infrared electromagnetic regimes [49], chemical robustness [69] and flat molded surface [70, 71]. Section 2.4 details the fabrication recipe for thin and flat slabs of PDMS. The inherent hydrophobic nature of PDMS with water contact angles of 103° [70] causes issues with the traditional interfacial assembly process described above. A control interfacial assembly with a hydrophobic PDMS slab and an oxygen plasma-treated PDMS slab illustrates this issue. Oxygen plasma descum treatment at 150 W for 1 min [72] temporarily yields the surface of PDMS as hydrophilic (Figure 2.4a). Figure 2.4b shows the results of the colloidal assembly. Harsh contact angles and dewetting forces lead to no coverage

of the hydrophobic surface compared to the hydrophilic surface. However, oxygen plasma treatment induces cracks in the PDMS surface, as shown in Figure 2.4c, which are detrimental for stretching applications.

Placing the target substrate above the water surface and dipping the substrate into the bulk of the sub-phase achieves smaller contact angles on hydrophobic samples [73]. This variant for air-water interfacial assembly is shown in Figure 2.5a. The substrate is inverted and placed above the water surface. The colloidal mask self-assembly process on the air-water interface is identical to the method described above. The first step in the mask transfer process onto the target substrate requires the addition of DI to the trough using a syringe pump. This step is continued until the PDMS substrate is fully submerged. At this point, DI is removed from the trough by the syringe pump to extract the PDMS substrate. After the assembly, the substrates are dried in the air overnight. Figure 2.5b shows a PDMS substrate after the successful assembly of a colloidal mask, and Figure 2.5c details the structure of the resultant colloidal mask. The colloidal mask was not coated with a metal layer for SEM characterization. This resulted in charging issues under standard secondary electron imaging due to the insulating nature of the PDMS substrate. The large dewetting forces from water on PDMS lead to contraction of the crystal with a spherical drying front and a resultant hole in the mask layer. The resultant mask layer has a higher density of line defects as compared to assembled masks on silicon substrates.

Smooth and reliable transfer [56] of the colloidal crystal using polymer rings is also explored. A generalized home-built ring confinement setup is shown in Figure 2.6a. The use of a confining ring allows the colloidal crystal fabrication process to be completely independent of the substrate surface chemistry. Another benefit is the ability to flush out submerged spheres using the outlet pipe. It is noted that the hydrophobicity and the weight of the ring depress the air-water interface, thereby increasing the capillary attraction forces inside the ring. This phenomenon has been investigated for other macroscale objects [65, 74]. Precise quantitative measurement of the surface tension can be made using a De Nouy method [75]. The elevated capillary attraction forces stabilize the colloidal crystal once the crystal packing approaches from loose-packed to close-packed. Figure 2.6b shows a photograph of the colloidal mask layer deposited on a shaped PDMS substrate. The large dewetting forces are not solved by this approach leading to large parts

of the substrate being non-coated and the mask layer cracking (Figure 2.7). Proposed solutions for this issue are making PDMS substrates hydrophilic by employing low-power oxygen plasma [76] or surfactants [77].

2.4 Methods

Interfacial assembly: The assembly recipe has been adapted from literature [73, 78–80]. Polystyrene sphere solution (1 µm, 10% wt.) (PSL) and sodium dodecyl sulfate (SDS) are purchased from Sigma Aldrich. A colloidal solution is made by mixing a 1:1 ratio of PSL and ethanol. A 4-inch petri dish is used as the assembly trough. Silicon <100> wafers are purchased from University Wafer Inc. The wafers are scribed to shape, degreased, and plasma cleaned using oxygen plasma at 150 W for 5 mins. The trough is filled with DI, and the target wafer is placed at the bottom. Small droplets of the colloidal solution (2-4 µl) are pipetted onto inch by inch-sized transfer silicon wafers. The wafers are dipped into the volume of the DI to transfer the spheres to the air-water interface. Once sufficient air-water interface area is packed with a loose-packed colloidal crystal layer, 3 µl of 2% SDS is pipetted directly onto the interface. This results in a closed-packed colloidal crystal layer. This layer is transferred to the target wafer by pipetting out the DI using the syringe pump. A small block is placed under one edge of the trough to tilt the trough by 5^{o} and achieve a linear drying front. The target wafer is allowed to dry in the air overnight.

Ring confinement recipe: Home-built assembly setup is laser cut out of acrylic sheets purchased from Mcmaster Carr Inc. Silicone o-rings (1/8" thick) are purchased from Mcmaster Carr Inc. All the components of the assembly setup are degreased with isopropanol and DI before use. Polystyrene sphere solution (1 µm, 10% wt.) (PSL) is purchased from Alfa Aesar Inc. The colloidal solution comprises 3:1:1 parts of propylene glycol, PSL, and methanol, respectively. The inlet pipe flow rate and outlet pipe flow rate are matched to obtain a stable water level. The silicone ring is placed on the air-water interface at the corner closest to the outlet pipe. The colloidal solution is dispensed slowly using a 50 µl microsyringe angled toward the outlet pipe. The dispense rate (3 µl/s) is adjusted to obtain the necessary compaction using Marangoni forces. The water flow also contributes a small

drift velocity toward the outlet pipe. The crystal is allowed to optimize under external perturbations for 5 minutes, and the submerged spheres are drained simultaneously. The silicone ring is carefully repositioned over the target substrate. The water level is decreased by closing the inlet and outlet pipes and opening the drain pipe. The colloidal crystal is allowed to deposit gently on the PDMS substrate. The PDMS substrate dries in the air at room temperature.

Scanning electron microscopy: Scanning electron microscopy is done on the FEI Quanta FEG 450 ESEM with high-vac mode (10^{-6} torr), 10 kV accelerating voltage, Everhart-Thornley secondary electron detector, 7 mm working distance, 20 µs dwell time, and 3.0 spot size.

Polydimethylsiloxane (PDMS) substrate fabrication: Sylgard 184 PDMS and trichloro(1H,1H,2H,2H-perfluorooctyl)silane are purchased from Dow Corning and Sigma Aldrich respectively. The masters (silicon wafers or glass slides) for curing flat PDMS slabs are silanized to enable easy and defect-free release of the PDMS slabs [81]. The master wafers are cleaned by solvent degrease and oxygen plasma treatment at 150 W for 5 mins. The cleaned wafers and an aluminum container with a few drops of trichloro(1H, 1H, 2H, 2H-perfluorooctyl)silane are pumped down to a low vacuum for 3 hours. This results in silane vapor deposition on the wafer surface and self-assembly of a silane monolayer yielding the master wafer surface superhydrophobic [81]. After extraction, the master wafer is optionally baked at 150 °C. The success of the process is verified by visually measuring the change in the contact angle of a water droplet on the wafer surface. The PDMS curing setup shown in Figure 2.8a consists of a 4-inch polystyrene petri dish cover, a Parafilm wax film liner, and a silanized master wafer. Parafilm wax liners prevent unwanted adhesion of the cured PDMS film to the petri dish cover. Dow Corning 184 Sylgard PDMS base and cure are mixed vigorously in a ratio of 10:1, respectively. Total weight of 15 g of PDMS mix results in a thin 1-2 mm thickness cured PDMS slab. The PDMS mix is poured inside the curing setup and degassed at a low vacuum to remove the air bubbles incorporated during the mixing step. The degassed PDMS mix is cured at 60 °C overnight. It is important to note that the curing temperature and curing time affect the cured films Young's modulus [82]. After curing, a 2.5" by 1.5" slab is cut from the top of the glass slide using an Exacto knife. The PDMS slab can be shaped as needed. The master wafer can be reused while

the rest of the setup is discarded.

The PDMS slab is shaped in to a dumbbell-shaped sample as shown in Figure 2.8b in order to achieve optimal straining. This is achieved by laser cutting the PDMS slab using a Epilog Laser Fusion laser cutter. Alternatively, the slab can also be hand cut using an Exacto knife. However, hand cutting requires extra care so as to not introduce fraying into the sides of the PDMS sample, which eventually lead to sample failure during straining. The cut PDMS samples are cleaned using detergent soap followed by solvent degrease. The PDMS samples are allowed to degas overnight inside a fume hood.

2.5 Figures

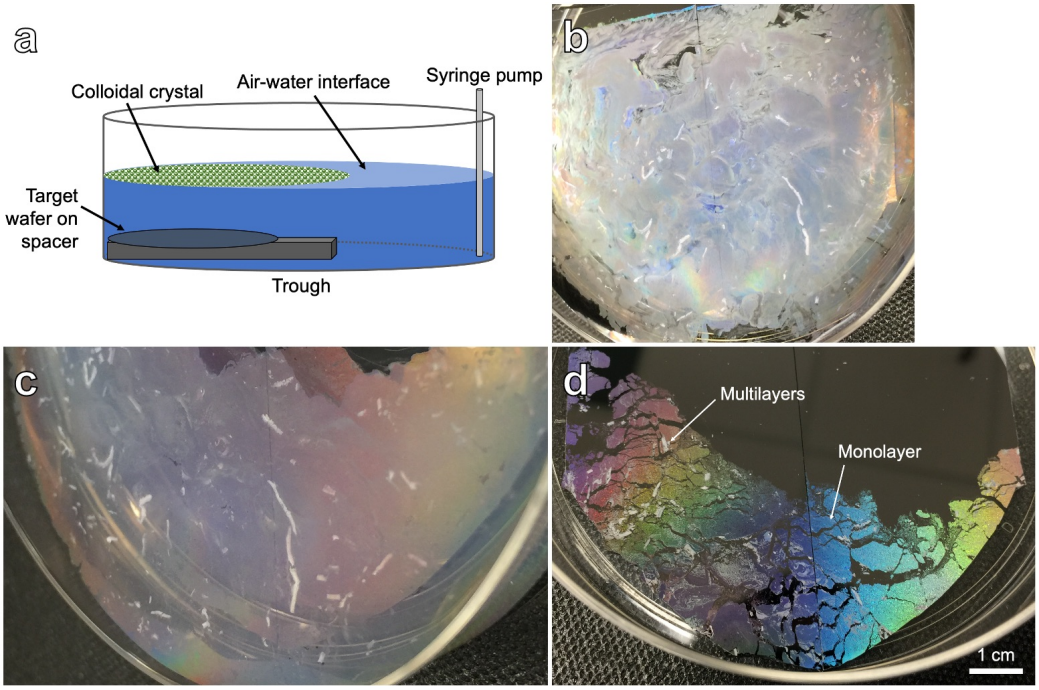

Figure 2.1: (a) Purpose-built assembly setup, (b) Unordered sphere layer on the water surface, (c) Ordered sphere layer on the water surface, (d) Large-scale assembly on a silicon wafer.

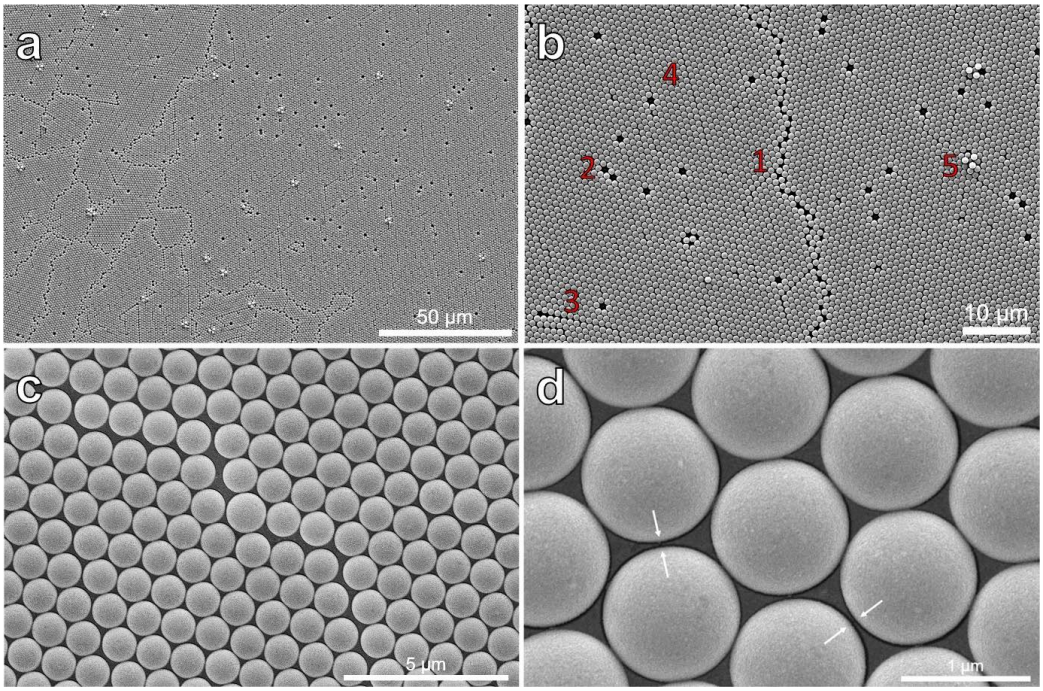

Figure 2.2: (a) Colloidal mask grains, (b) Crystal defects (1 - grain boundary, 2 - vacancy defect, 3 - line defect, 4 - evaporation-induced line defect, 5 - triplet defect), (c) Larger diameter sphere leading to line defect generation, (d) Smaller diameter spheres causing gaps. The colloidal crystal is coated with a 30 nm gold layer.

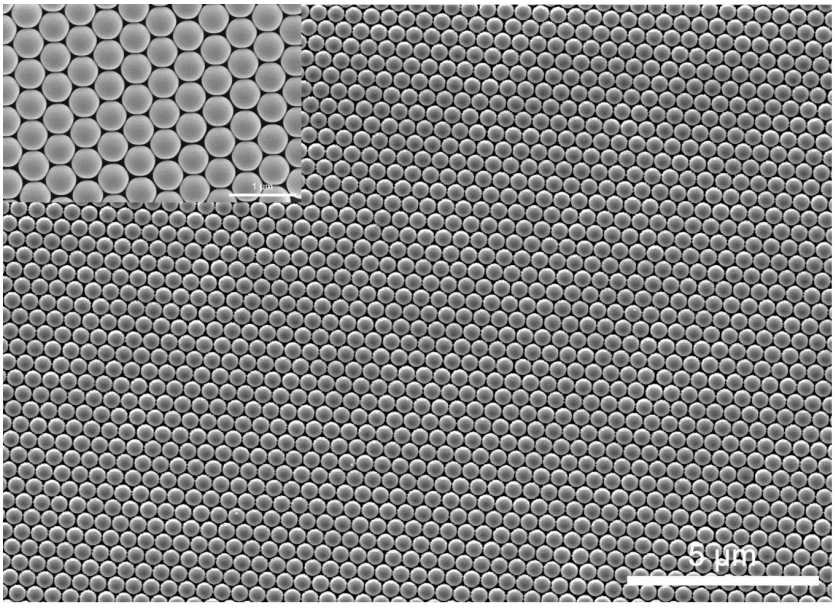

Figure 2.3: Colloidal mask of 500 nm diameter polystyrene spheres.

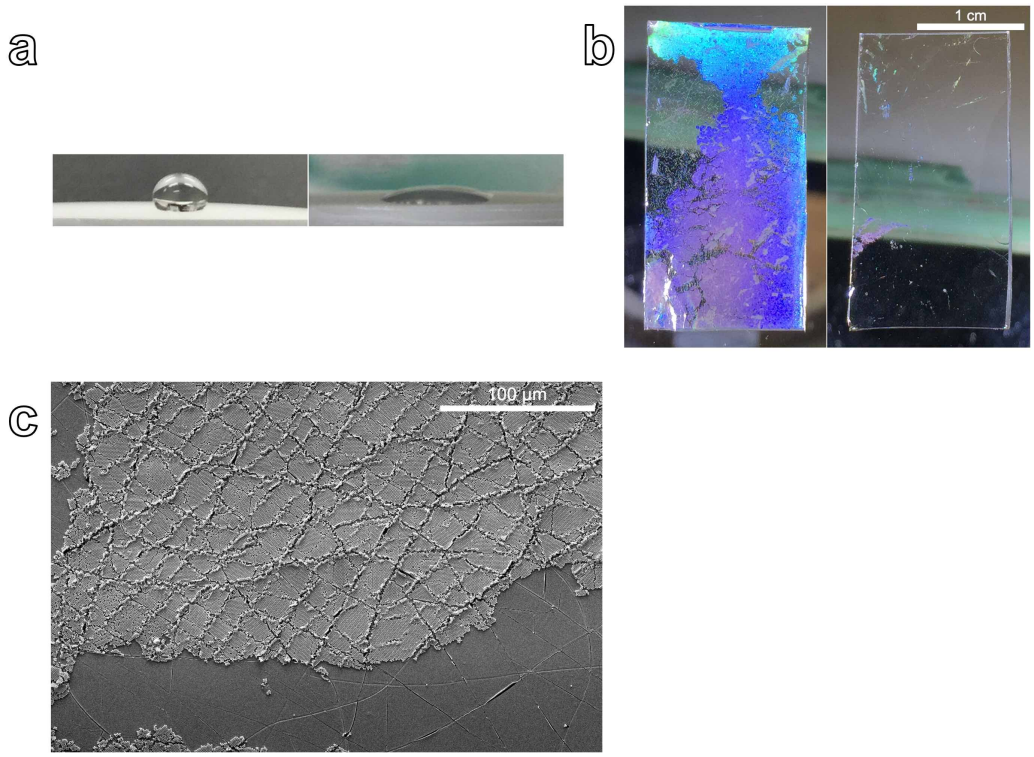

Figure 2.4: (a) Water droplet on PDMS (left) vs. water droplet on oxygen plasma treated PDMS (right). Oxygen plasma treatment is performed at 150 W for 60 s, (b) Centimeter scale coverage for hydrophilic PDMS (left) vs. minimal coverage for PDMS (right), (c) Surface cracking due to oxygen plasma treatment.

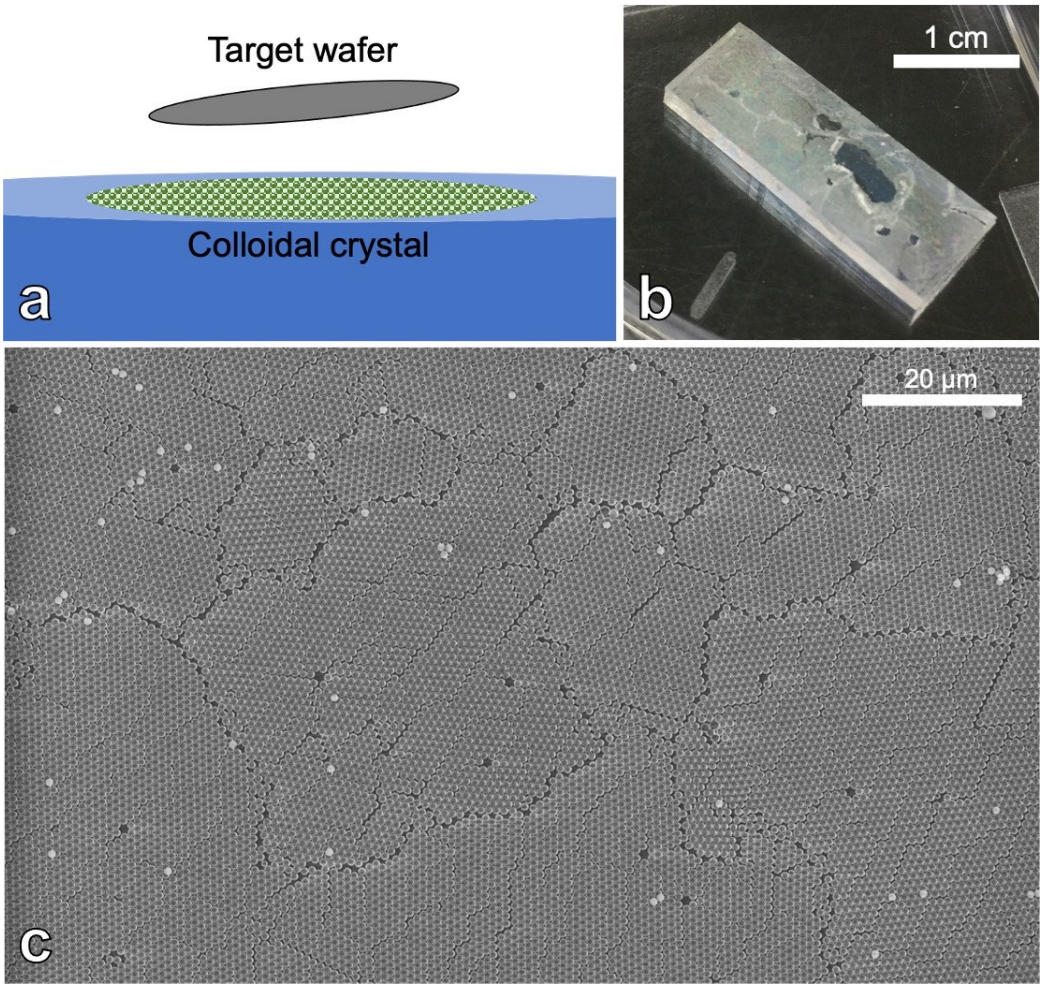

Figure 2.5: (a) Wafer placement with respect to the air-water interface for assembly on hydrophobic substrates, (b) PDMS sample with an assembled colloidal mask layer, (c) Large-area SEM of the uncoated colloidal mask.

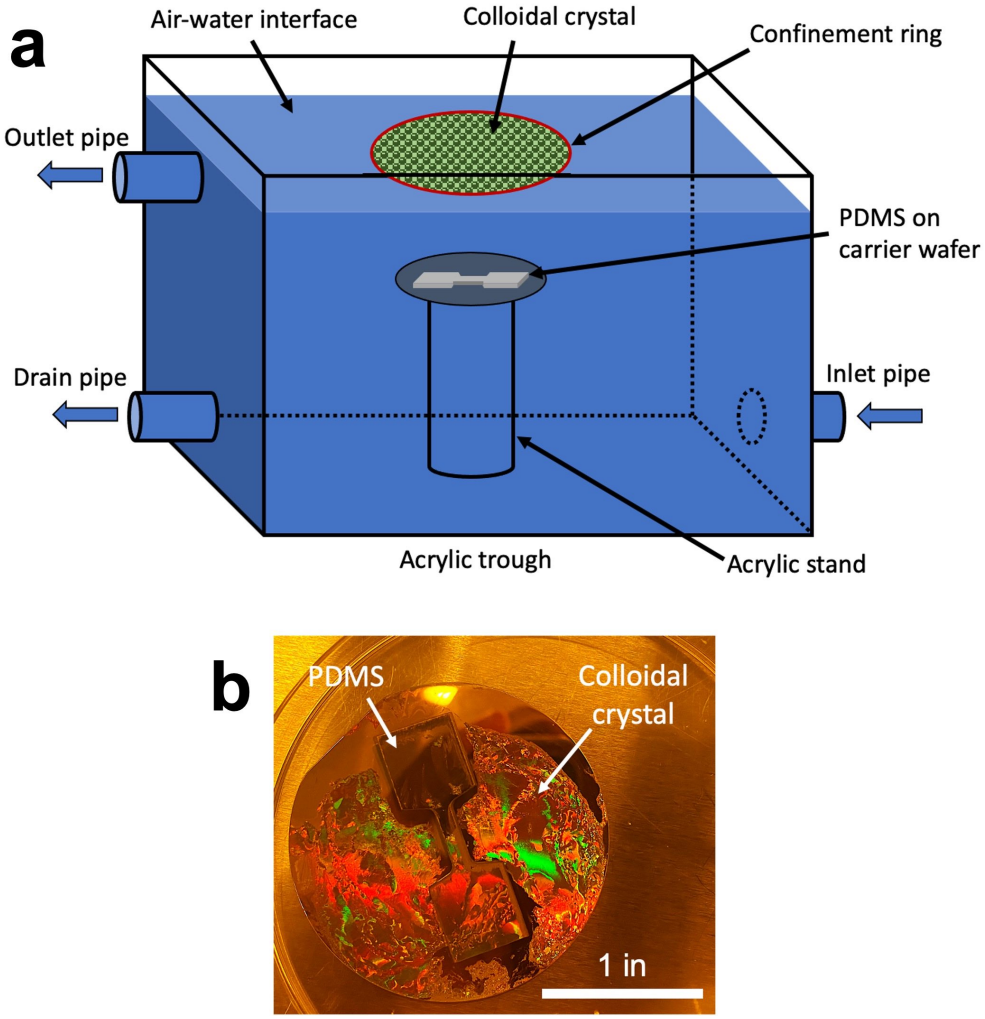

Figure 2.6: (a) Generalized ring confinement setup, (b) Resultant deposition on a shaped PDMS substrate.

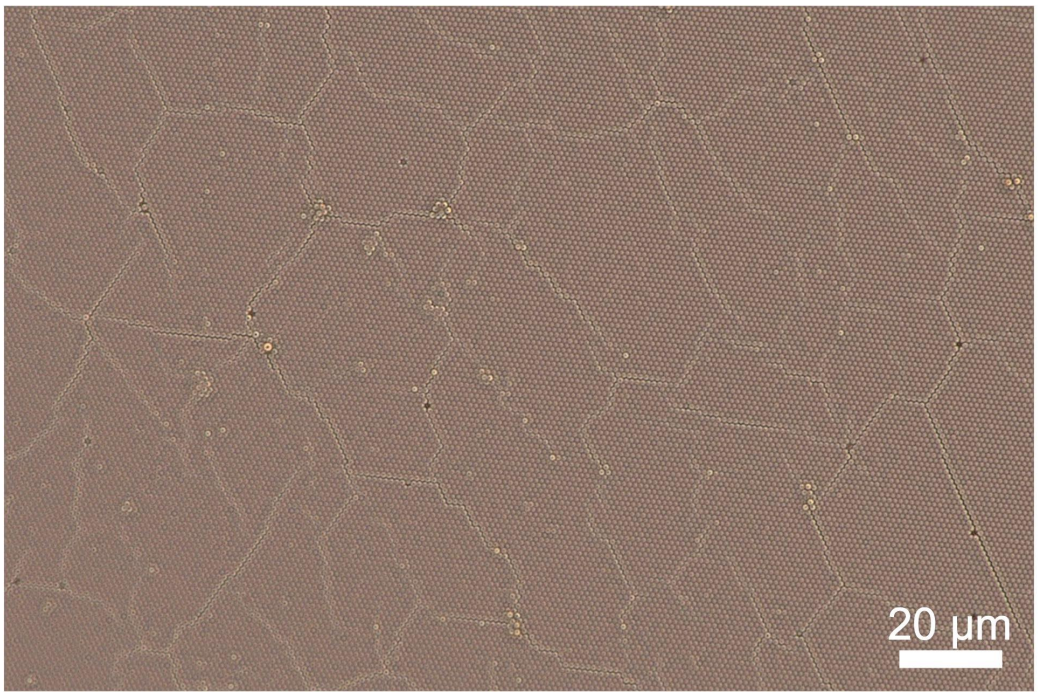

Figure 2.7: Optical microscopy image of cracked colloidal monolayer on PDMS.

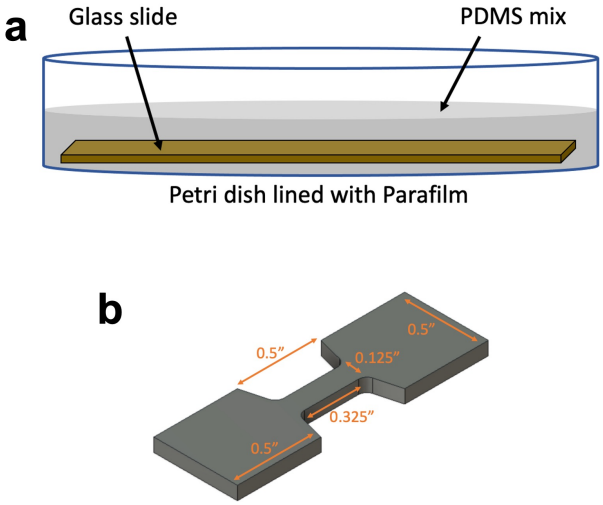

Figure 2.8: (a) Curing setup, (b) Shaped PDMS sample.

CHAPTER 3

UNLOCKING LARGE-AREA LOW-DEFECT COLLOIDAL MASKS

3.1 Mask Fabrication

Figure 3.1a shows the purpose-built assembly setup. The setup comprises a silicon wafer coated with a DI layer and a front-open acrylic enclosure with a variable speed inlet fan and an acoustic exciter. As illustrated in Figure 3.1b, the colloidal solution is dispensed at the edge of the silicon wafer. The dispensed spheres inject into the DI layer, get transported toward the air-water interface due to the rapid evaporation of the IPA solvent, and readily adsorb on the interface [83, 84]. As the concentration of the spheres at the interface increases, sphere aggregation occurs due to Marangoni convection [64]. These primary aggregates are reoriented by external energy sources to eliminate grain boundary generation [54, 55]. The silicon substrate plays a crucial role in this purpose. The planar and circular nature of the wafer allows easy external energy integration with low-velocity air currents parallel to the surface and acoustic vibrations coupling through the wafer base. The combination of tangential (air) and radial nanosphere transport (acoustic) provides an ideal crystal optimization strategy. The hydrophilic-hydrophobic boundary at the edge of the wafer naturally confines the external and the surface tension forces. This allows the self-assembly of the colloidal mask layer directly on top of the target substrate, eliminating defect generation encountered during the mask transfer process to the target substrate [56].

The self-assembly process continues until the formation of a single large-area quasi-single crystal. The low volume fraction (2.31%) of the spheres in the colloidal solution enables the formation of a monolayer instead of multilayers. At this point, the external energy sources are switched off. The colloidal crystal is assembled on the silicon wafer by draining the DI layer. This step also eliminates the nanospheres that previously escaped the solvent

evaporation convective flow and stabilized in the DI layer. These submerged nanospheres are known to cause triplet defects in two-dimensional colloidal crystals [55, 61]. The resultant large-area quasi-single crystal is shown in Figure 3.1c.

The circular symmetric external energy input and a lack of global boundary condition lead to a circular symmetric twist in the large quasi-single crystal. This phenomenon is verified by twist measurement using a scanning laser diffraction setup shown in Figure 3.2a. The inch-scale quasi-single crystal from Figure 3.1c is exposed to a HeNe laser, and the resulting diffraction pattern is recorded on a screen. As the laser spot is moved along cross-section lines over the colloidal crystal (six lines are shown in Figure 3.2b), the rotation of the diffraction pattern gives the change in the relative crystal orientation. The high level of hexagonal crystal symmetry is demonstrated by the crisp diffraction spots shown in the inset of Figure 3.2b. Figure 3.2c maps the relative crystal orientation as the laser spot moves along the y = 0 mm path. The sharp change in the orientation toward the end of the path indicates a line defect. This effect can be qualitatively observed with the large line defect marked in Figure 3.2b. Figure 3.2d maps the relative crystal orientation for all of the measurement paths. The roughness in the curves is attributed to image processing errors. The crystal twist varies by less than 0.5^o per mm at the center of the colloidal crystal.

3.2 Importance of Nanosphere Surface Properties

Literature [55, 61, 64, 74, 85–87] has established that the formation of large-area defect-free crystal grains requires careful tuning of the attractive and the repulsive forces existing between colloidal nanospheres. The relevant attractive forces are hydrophobic-hydrophobic interactions, while relevant repulsive forces are steric repulsion and electrostatic forces. The capillary attraction forces and gravity forces are negligible for the small diameter nanospheres in this thesis. Compaction is achieved using Marangoni convection and external forces.

As received, the steric repulsion and electrostatic repulsion due to added anionic surfactants stabilize colloidal spheres. Here, a simple strategy for optimization of the colloidal solution chemistry is presented. The most basic

solution would have a high vapor pressure alcohol, i.e., isopropanol and 10% wt. polystyrene sphere solution (PSL). Figure 3.3 shows the microscopic characterization of a sample made using 4:1 isopropanol and PSL solution. The monolayer mask is composed of 10 to 150 µm lateral-sized grains with random orientations. It is confirmed that the compaction forces are not able to fully overcome the entropic gains due to hydrophobic-hydrophobic interactions [64]. As a result, the grains do not reorient during the crystal compaction process. This is confirmed by taking fast Fourier transforms (FFT) of the SEM images, which showcase closed rings instead of a hexagonal dot pattern.

Hydrophobic-hydrophobic interactions are mediated by increasing the hydrophilicity of the polymer spheres, thereby reducing the available hydrogen bonding sites for water molecules [64, 66, 74]. This has been achieved with surface treatments with alcohols [64, 85, 86] or surfactants [55, 61]. Here, the use of a low-vapor pressure dihydric alcohol, propylene glycol (PG), is explored. PG and its counterpart ethylene glycol possess two O-H groups and a small hydrophobic carbon chain. They also feature very low vapor pressures, have been shown to wet polystyrene surfaces more than water [88], and are frequently employed as emulsion stabilizers for oil-in-water systems [89]. In the presence of surfactants or solid particles, glycols readily adsorb on the surfactant headgroup at hydrophilic-hydrophobic boundaries, disrupting water molecules' ability to form hydrogen bonds with hydrophobic portions of solutes and act as co-surfactants to help increase hydrophilicity [90–92]. The choice for PG is made due to its equivalent density to polystyrene, higher vapor pressure to expedite drying time, and lower viscosity to achieve effective colloidal solution injection. The viscosity is further adjusted by adding DI to the colloidal solution. Figure 3.4 demonstrates the ability of PG to increase the hydrophilicity of polystyrene surfaces. The static contact angle decreases from 87^o to 69^o with increasing PG concentrations from 0% to 0.9%. The selected PG concentration in the self-assembly setup is roughly 0.4%. It is worth noting that an increase in colloidal hydrophilicity increases the chances of colloidal spheres escaping the convective flow toward the air-water interface [55]. Figure 3.5 shows the improved large-area quasi-single crystal mask made from the PG-based recipe. This recipe is referred to as DIPGIP. The crisp hexagonal dot pattern in the FFT analysis validates the elimination of grain boundaries and the existence of high hexagonal order.

SEM edge effects can be employed for visualization of the smaller defects typically ignored in large-area analysis. Figure 3.6 shows the ability of SEM imaging to highlight the defects in a monolayer colloidal mask layer. This effect is especially pronounced for uncoated mask layers as a higher number of secondary electrons escape from the defect sites as compared to the neighboring perfect crystal [93]. These defect patterns match perfectly with the results from the defect density quantification algorithm (Figure 3.7a,b). The defect density is quantified using a MATLAB algorithm derived from the pair correlation function approach [56]. The large-area SEM scans are processed using circular Hough transform and Delaunay triangulation to create a triangular mesh connecting the sphere centers. The distance between neighboring spheres is measured against a range of 105 nm around the mean sphere diameter. If the distance falls outside the range, then a defect is detected.

The defects in the colloidal crystal are analogous to atomic crystal defects. The colloidal crystal possesses point defects, such as miscoordinated spheres, monovacancies, divacancies, multilayer triplet defects, and dendritic line defects. These defects are labeled in Figure 3.7c. Point defects like miscoordinated spheres and vacancies are caused by the colloidal sphere size and shape polydispersity [94–96]. Triplet defects are generated by submerged spheres pushing up on the monolayer crystal during the drying process [55, 61]. The displaced spheres reconstruct into a triplet formation. The dendritic line defects are caused by the ultra-fast crystal lattice transformation due to the evaporation of water [62, 97]. Further processing steps are required to eliminate these line defects as shown in the next section.

3.3 Solvent Annealing

Solvent annealing treatment of colloidal crystals leads to a significant reduction in the line defect density [62]. This technique applies an aerosolized solvent gas to the colloidal crystal on the air-water interface before extraction. The polymer chains on the spheres absorb the solvent molecules, migrate over to the contact points with the neighboring spheres and fuse with other polymer chains to minimize their surface free energy. This process results in the creation of a crack-resistant two-dimensional colloidal crystal film.

The aerosolized solvent vapor is produced by passing a carrier nitrogen gas through commercially available acrylic cement. The resultant vapor contains trichloroethylene, which readily dissolves polystyrene [62, 98]. Figure 3.8a shows the solvent annealing chamber that functions as an add-on module for the assembly setup shown in Figure 3.1a. The chamber is designed as a diffusive settling chamber that achieves a uniform concentration of solvent vapor. The colloidal crystals are treated for 16 mins at 2 scfh flow rates. There is no visual change observed in the macroscale photographs of the crystals. However, the movement of the colloidal crystal post-treatment mimics a two-dimensional layer, which suggests a successful annealing process.

Figure 3.8c shows the FFT analysis of SEM scans taken three at random locations. As expected, the results portray a high degree of uniform hexagonal ordering. Both metal coated and uncoated SEM scans in Figures 3.8d, 3.9 and 3.10a,b demonstrate significant reduction in dendritic line defect length and density, however, no reduction in point-source (miscoordinated spheres, vacancies, and triplets) defects is observed. Therefore, it can be concluded that the sphere linking process due to solvent annealing impedes the propagation of line defects away from the point defects. A close-up scan of a large sphere point defect is shown for both an untreated and a solvent treated crystal is given in Figure 3.10c as proof.

The mean defect density of solvent treated samples (Figure 3.10d) shows improvement by a factor of 15x and 5x as compared to the control (4:1 isopropanol and PSL) and untreated samples, respectively. Further improvement resulting in low disorder ($< 1\%$) colloidal crystals would require minimizing the nanosphere diameter variation in the commercial PSL solution.

3.4 Template Enforcement

The principle of boundary enforcement for single crystal fabrication has been shown for a single one-dimensional boundary [55, 99, 100]. This principle is intuitive as the colloidal crystal aligns with the meniscus edge between water and the external medium. In contrast to the literature reports, the self-assembled crystal in our process is not constrained against the boundary of the silicon wafer. The circular symmetry of the system is propagated throughout the colloidal crystal using external energy, i.e., circular confine-

ment of tangential transport from the airflow and radial transport from the acoustic vibrations. Therefore, a natural curiosity is investigating the relationship between the boundary shape and the long-range orientation in our colloidal crystals. This section shows that using a hexagonal template boundary enables single dominant crystal orientation enforcement through a large-area crystal. The assembly setup is shown in Figure 3.11a, where a low-cost hexagonal template is created by using Kapton tape (VWR Inc.). The external energy setup is not shown for simplicity. Due to a large difference in the wettability of the clean silicon oxide surface and the Kapton surface, the water thin film obeys the template boundaries even with the addition of energy sources. The resultant single crystal is shown in Figure 3.11b. It is observed that the colloidal crystal preferentially aligns with the symmetry lines perpendicular to the hexagonal template. Further verification of the single crystal orientation using laser diffraction measurement needs to be done. This assembly process will be employed for deterministic aligned assembly of the colloidal crystal on shaped substrates for angle-resolved nanosphere lithography applications.

3.5 Methods

Colloidal Mask Fabrication: The colloidal solution is prepared by mixing 1:3:3:2 parts of deionized water (DI): propylene glycol (PG): isopropanol (IPA): 10% wt. 1 µm polystyrene spheres (Alfa Aesar Inc.) (PSL), respectively. This recipe is henceforth called DIPGIP. The solution is ultrasonicated for 10 minutes. A clean 100 mm silicon wafer is placed inside the purpose-built colloidal assembly setup shown in Figure 3.1a. The setup enclosure houses an inlet fan (Thermaltake CPU fan) on the back wall and an acoustic exciter (Dayton Audio 40 W 4 Ω subwoofer) placed next to the wafer bench. The silicon wafer is coated with 10-11 ml of DI. The colloidal solution is dispensed at the edge of the silicon wafer in 3-5 µl droplets for a total volume of 105 µl. The air flow velocity at the face of the fan is set at 2.5-2.6 m/s. The acoustic exciter is driven using a function generator with 44 Hz, 1 Vpp, and 5 ms square pulses. The crystal reorientation is initiated with the solution dispense and continued for 3 hours following the dispense. During extraction, the external energy sources are switched off. The colloidal crystal

is compacted by breaking the water surface tension using a cleanroom wipe. The colloidal crystal is allowed to dry in the air for a few hours.

Solvent Annealing: Optimized colloidal crystals are solvent treated for 16 minutes using the home-built solvent annealing box shown in Figure 3.8a. Trichloroethylene is inlet into the solvent annealing box by bubbling nitrogen gas at 2 scfh through a glass bubbler containing Weld-On 4 acrylic cement (SCIGRIP Inc.). The crystal is extracted using the same procedure listed above.

Defect Measurement and Analysis: Large-area (6144 x 4415 pixel density) scanning electron microscopy (SEM) scans are obtained at random points in the quasi-single crystals using the FEI Quanta FEG 450 ESEM. The scan parameters are high-vac mode (10^{-6} torr), 10 kV accelerating voltage, Everhart-Thornley secondary electron detector, 5 mm working distance, and 800x magnification. Image processing is performed on the large-area SEM scans to determine the areal defect density in the mask layers. The SEM scans are processed with a circular Hough transform and Delaunay triangulation to create a triangular mesh connecting the sphere centers. The center-to-center links in the triangular mesh are measured against a range of 105 nm around the mean sphere diameter. If this condition is not met, then the triangle with the defective link is marked defective. Subsequently, the total defective area of the scan is computed by the sum of the individual triangle areas. Gap analysis is carried out using Gwyddion software and Python scripts. Fast Fourier transform (FFT) analysis is done using Image J software.

Twist Measurement and Analysis: The large-area twist measurement setup is shown in Figure 3.2a. The silicon wafer with a colloidal mask layer is rested on a manual microscope XY-stage. A Melles Griot 5 mW HeNe laser is mounted vertically, approximately 40 cm above the microscope stage, pointing downwards. A white paper screen with a circular hole, 4 mm in diameter, is fixed 5 mm above the microscope stage so that the HeNe laser beam passes precisely through the 4 mm hole in the screen. The silicon wafer, sitting on the microscope stage, the silicon wafer is the only moving object in the described experimental setup. A single lens and a Point Grey CCD camera are mounted above the screen and capture 20 mm x 20 mm of the central screen area onto the camera. A transformation function is applied to the captured spot patterns to account for the camera tilt. Subsequently, a ring enclosing the hexagonal spots is spliced along the θ polar coordinate.

The six-spot pattern leads to six peaks in the intensity vs. θ coordinate graph. Finally, the twist in the crystal is determined by the change in the θ coordinate of a chosen single spot as the laser moves through the colloidal crystal.

3.6 Figures

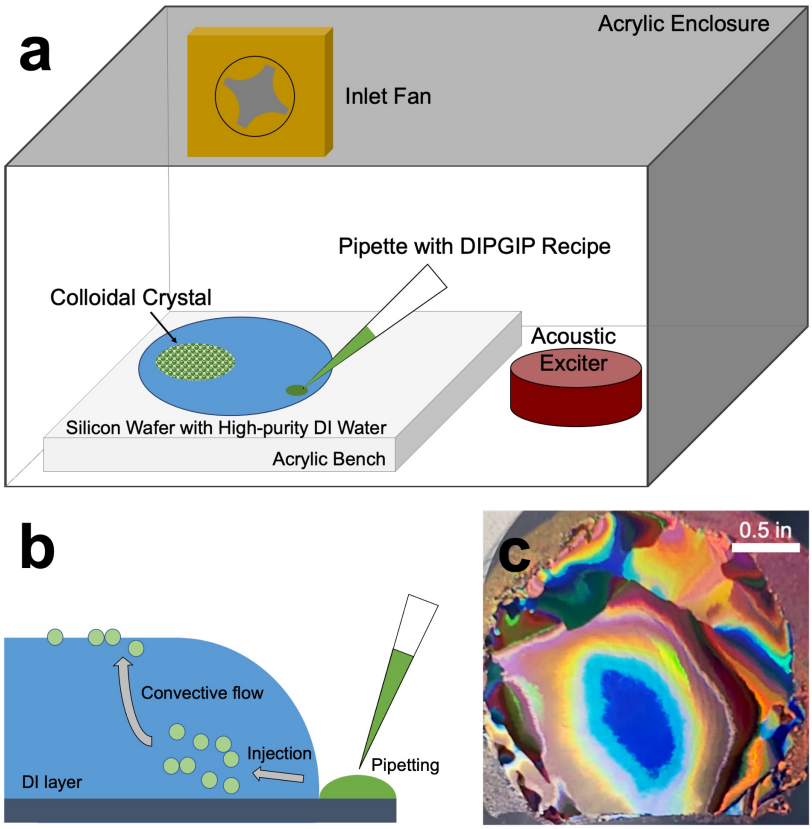

Figure 3.1: (a) Purpose-built assembly setup, (b) Sphere transport mechanism to the air-water interface, (c) Quasi single-crystal mask on a 100 mm diameter silicon wafer.

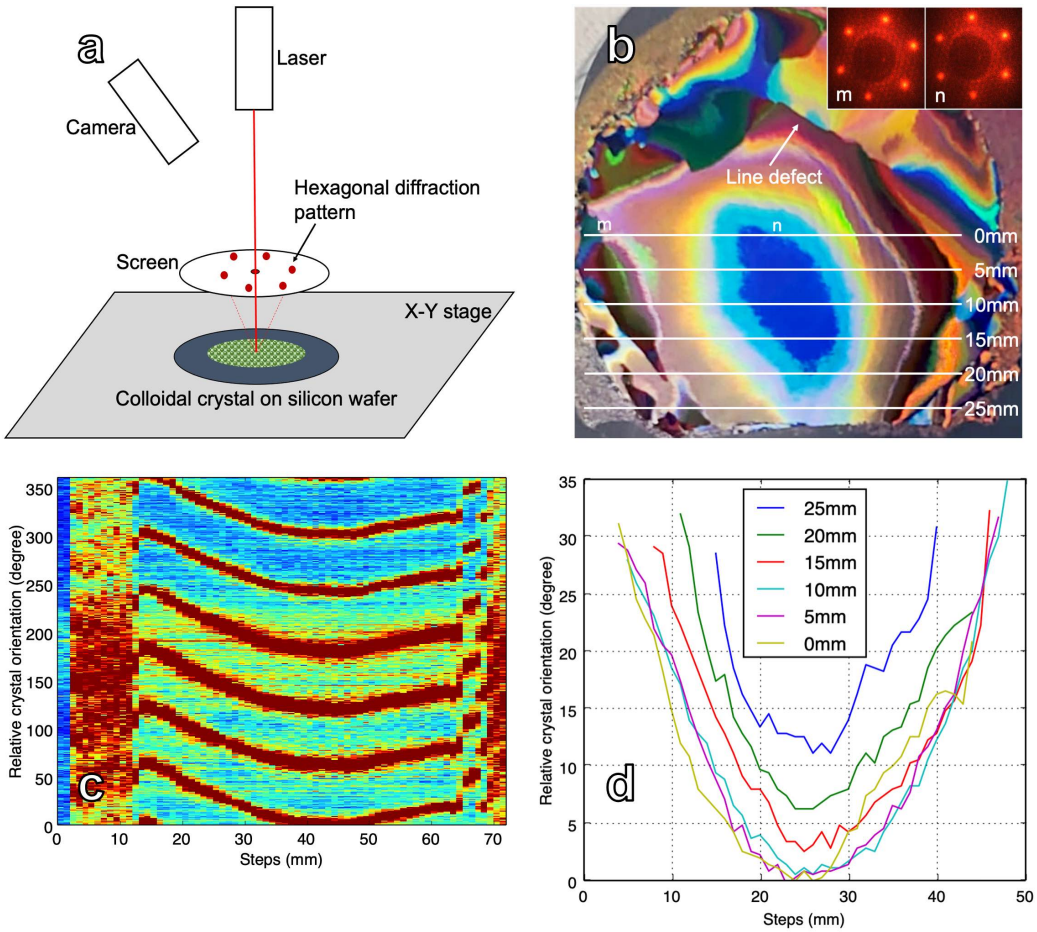

Figure 3.2: (a) Large area twist measurement setup, (b) Measurement paths: y = 0 mm, 5 mm, 10 mm, 15 mm, 20 mm and 25 mm (Inset: camera output demonstrating crystal twist between points m and n), (c) Relative crystal orientation along the y = 0 mm path. Each curve represents one diffraction spot. (d) Relative crystal orientation for all of the measurement paths.

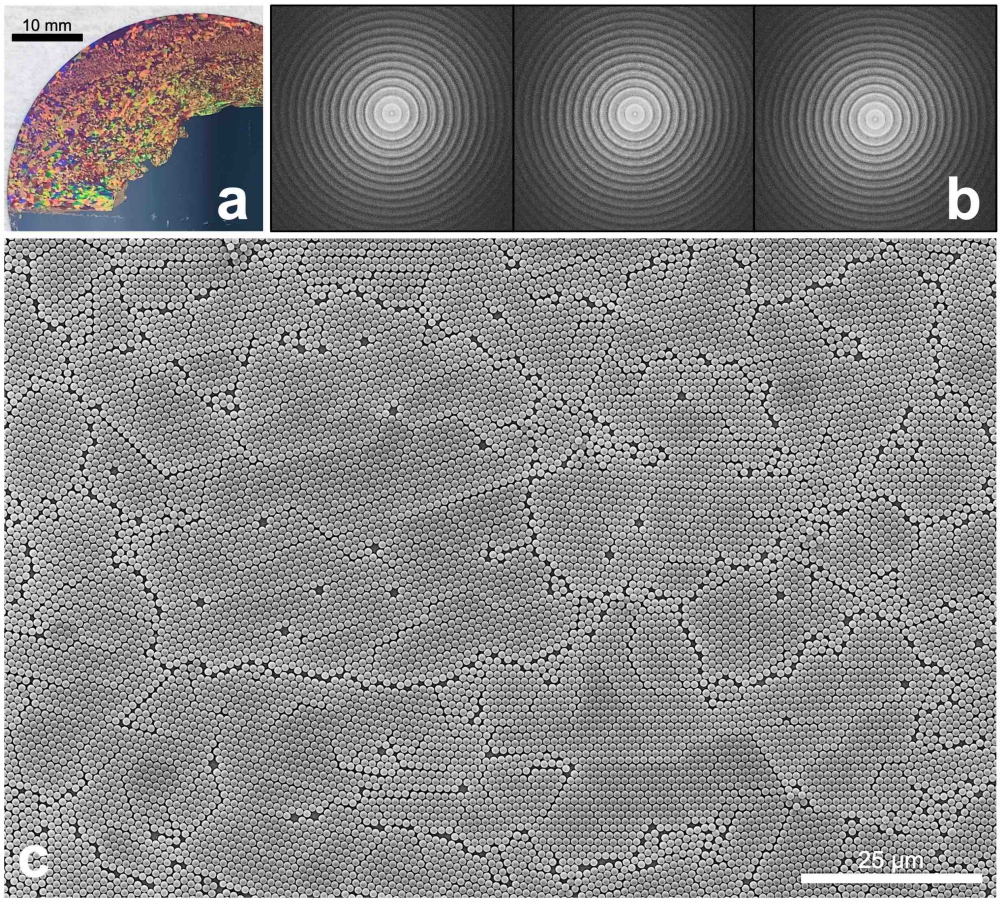

Figure 3.3: (a) Photograph of a 4:1 isopropanol and PSL sample, (b) FFT analysis on three large-area SEM scans, (c) Example of a large-area SEM scan of monolayer colloidal mask.

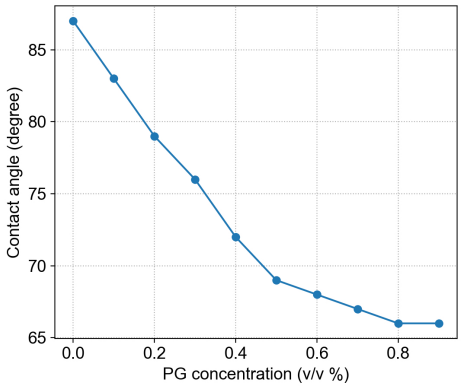

Figure 3.4: Static contact angle of PG aqueous solutions on a polystyrene surface.

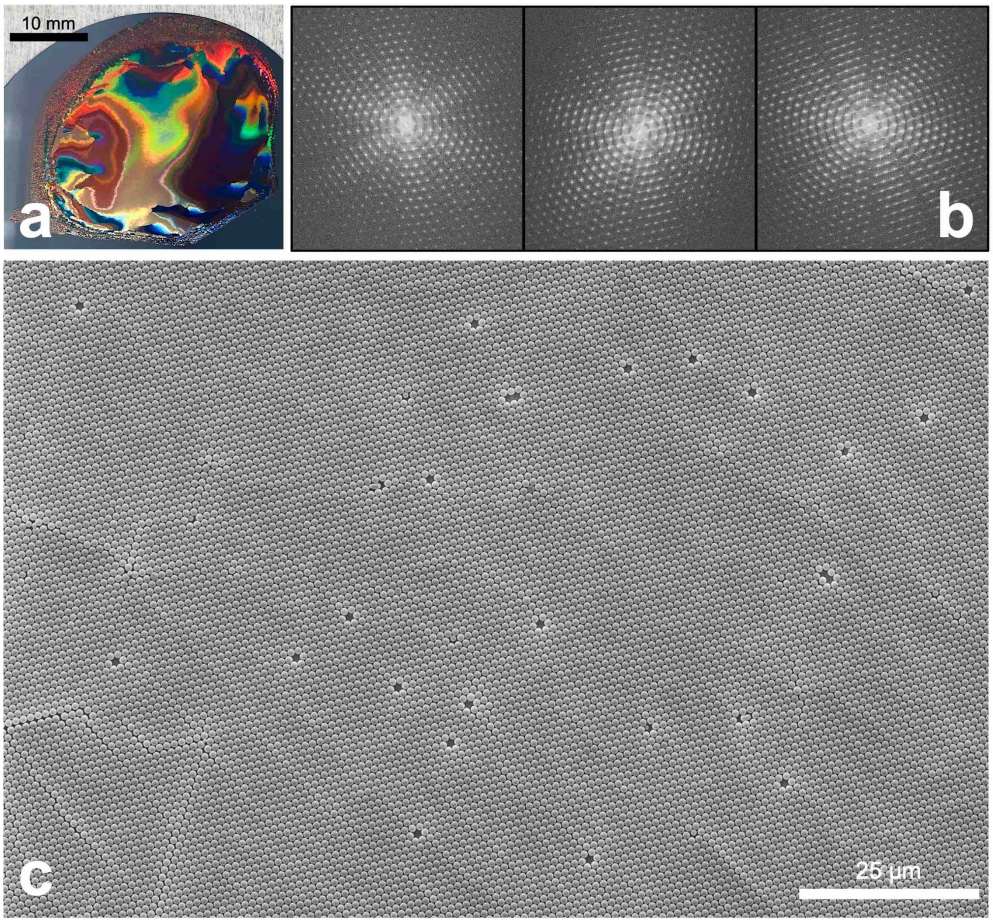

Figure 3.5: (a) Photograph of a sample made from DIPGIP recipe, (b) FFT analysis on three large-area SEM scans, (c) Example of a large-area SEM scan of the monolayer colloidal mask.

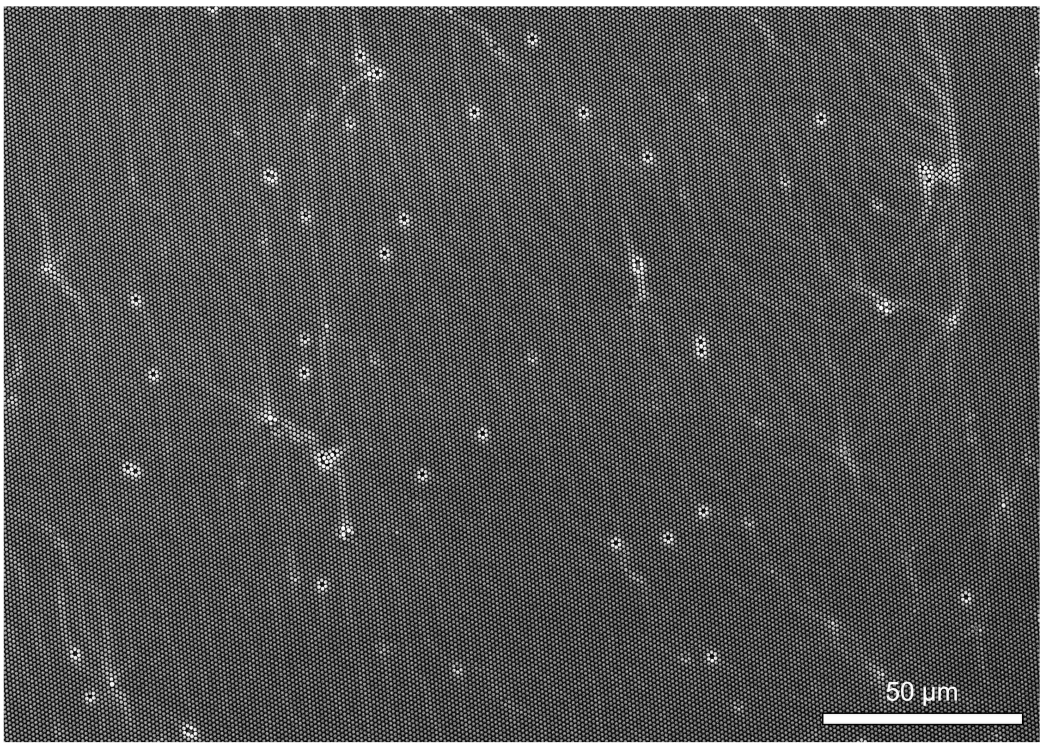

Figure 3.6: Large-area SEM image of a colloidal crystal without a metal layer.

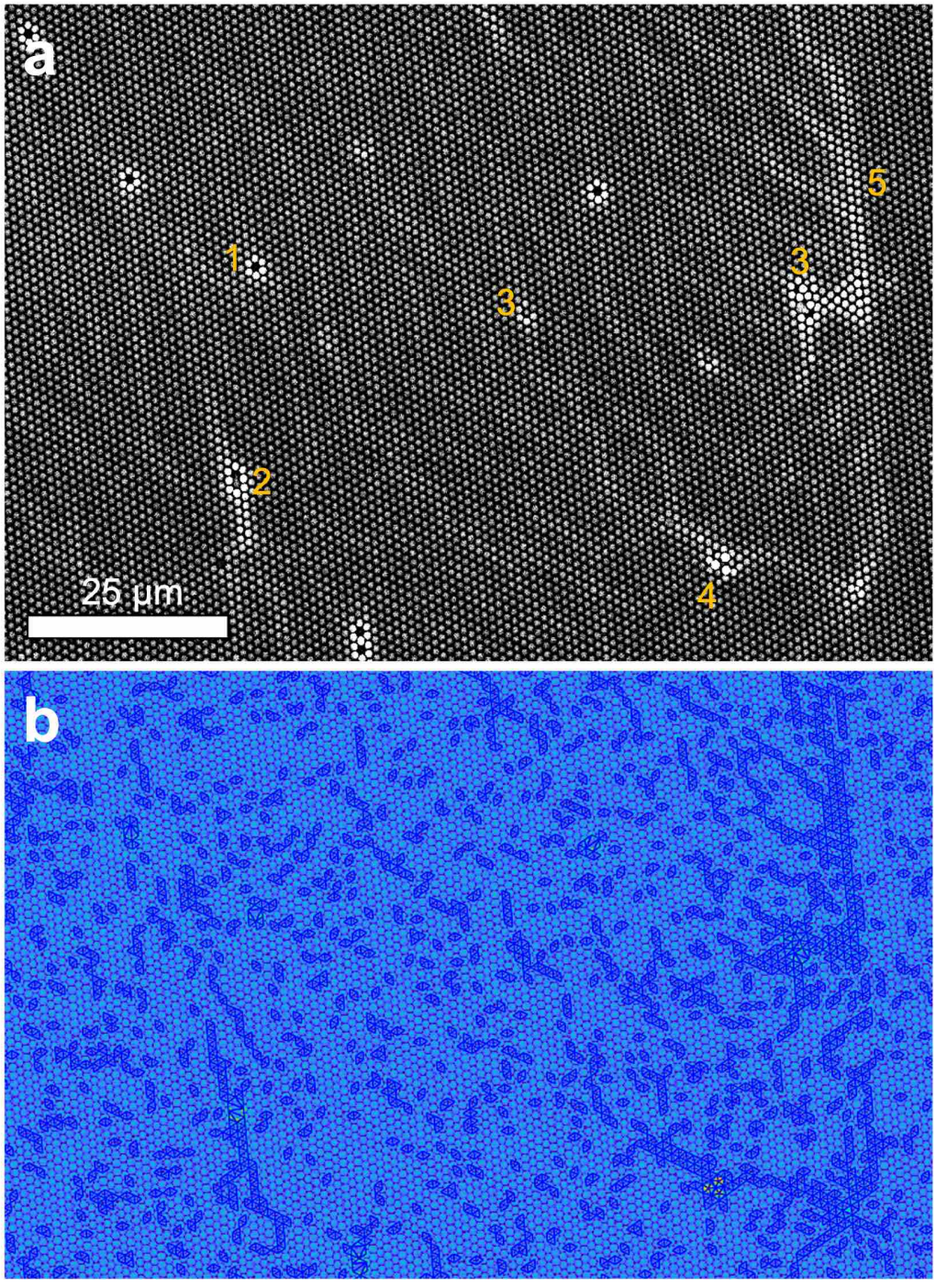

Figure 3.7: (a) Cropped image of Figure 3.6. Crystal defects are labeled, 1 - monovacancy, 2 - divacancy, 3 - miscoordinated spheres, 4 - triplet, 5 - line defects, (b) Algorithm processed image of Figure 3.7(a).

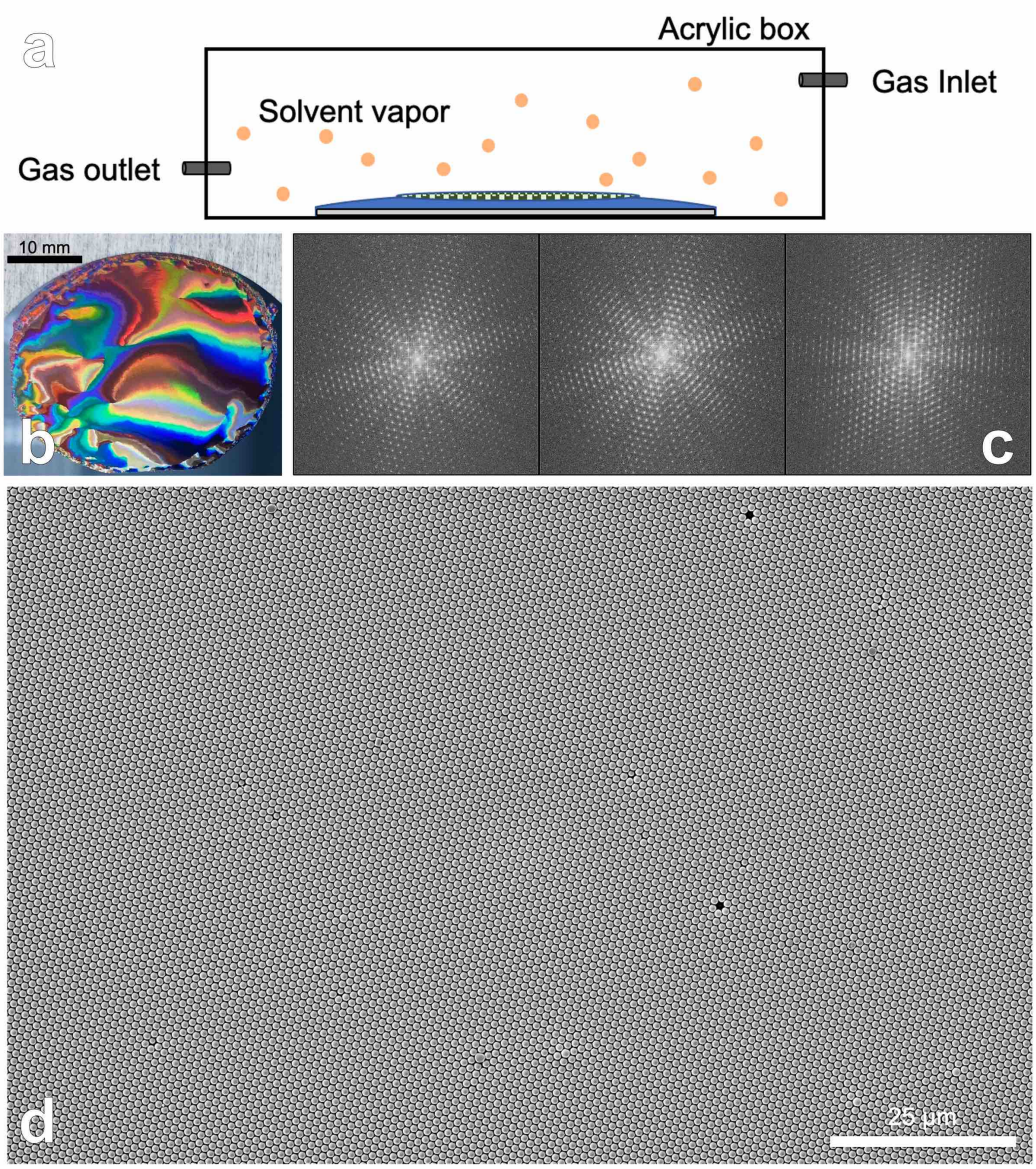

Figure 3.8: (a) Side-view schematic of the solvent annealing box, (b) Photograph of solvent annealed plus DIPGIP recipe sample, (c) FFT analysis of three large-area SEM scans, (d) An example of a large-area SEM scan.

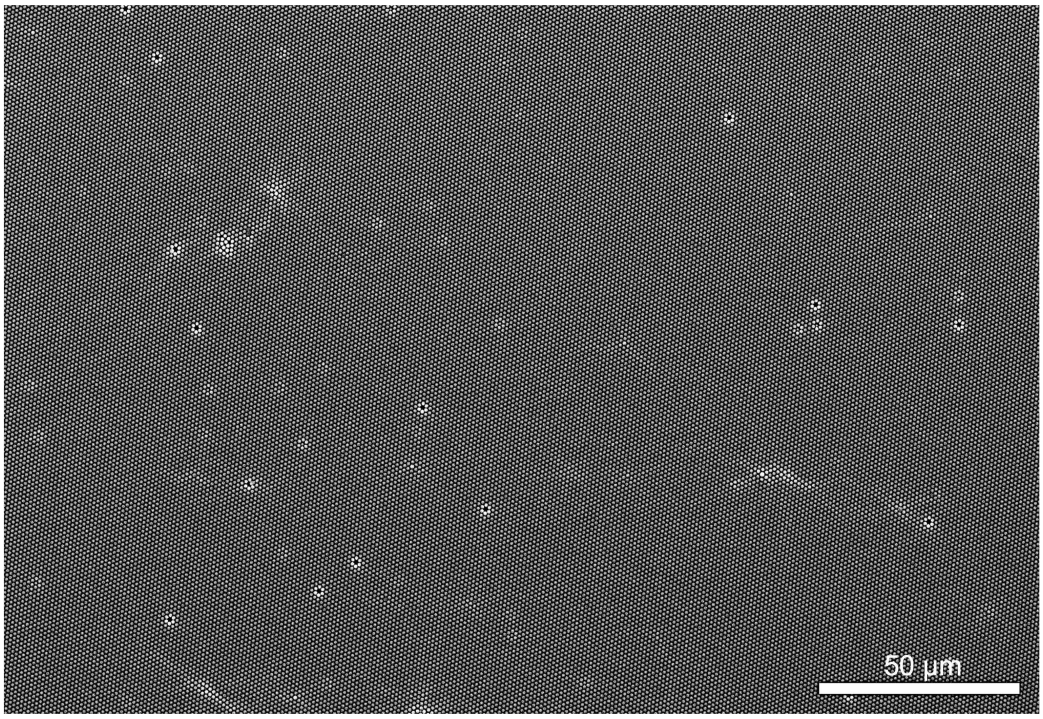

Figure 3.9: Large-area SEM image of a solvent treated colloidal crystal without a metal layer.

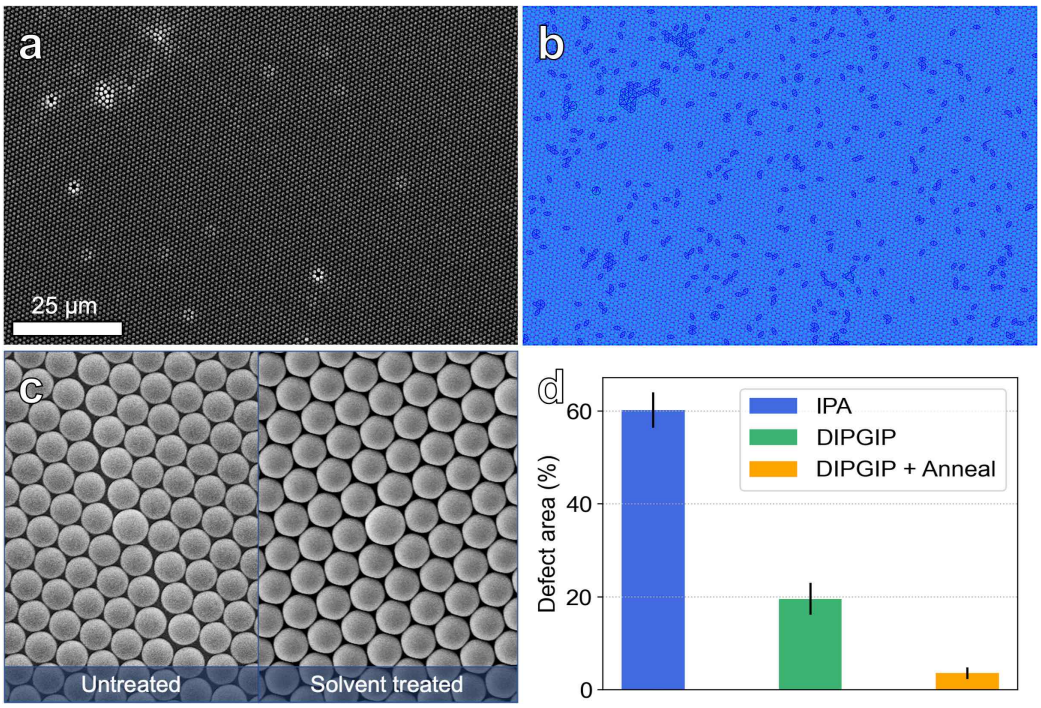

Figure 3.10: (a) Cropped image of Figure 3.9, (b): Algorithm processed image of Figure 3.10(a), (c) Crystal cracking around point defects for untreated crystals vs. solvent treated crystals, (d) Mean defect density for 10 large-area SEM scans of 4:1 IPA and PSL sample, DIPGIP recipe sample and DIPGIP plus solvent annealing recipe sample.

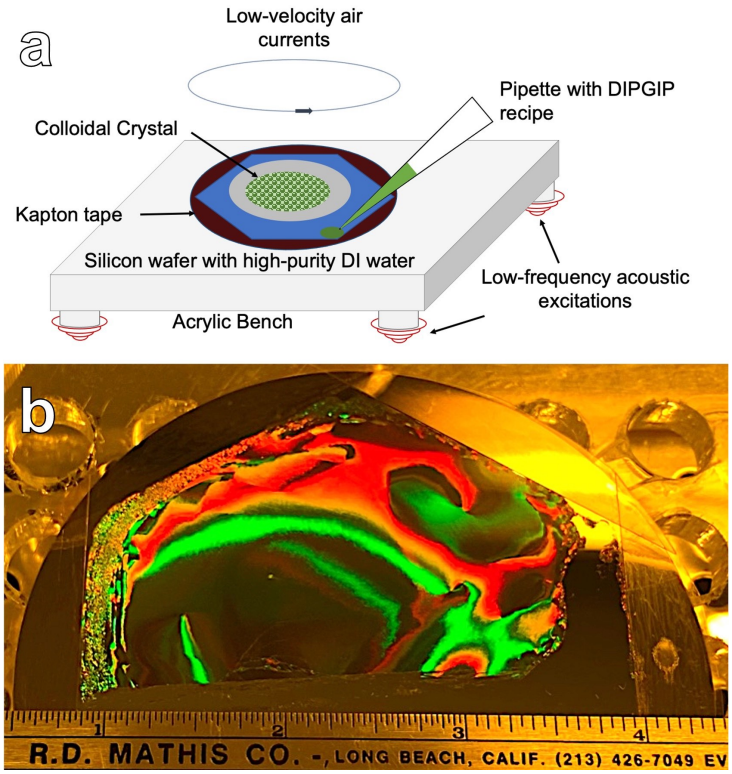

Figure 3.11: (a) Template based self-assembly setup, (b) Large-area single crystal colloidal mask.

CHAPTER 4

SENSOR CHARACTERISTICS

4.1 Nanoparticle Array

The colloidal mask fabrication is followed by a single step of thermal/electron beam evaporation to instantaneously fabricate hexagonally symmetric arrays of triangular nanoparticles (Figure 4.1a). The shape, size, and spacing of the array are dictated by the negative space in the mask, thereby the size of a single sphere. The theoretical relations between the diameter of an individual sphere, the resultant nanoparticle height, and the interparticle distance are given in Chapter 1. In practicality, the particle sizes are bigger, and the interparticle distances are smaller due to sphere polydispersity. The particles have sloped edges going from maximum thickness to the substrate over ~ 20 nm. Based on the measurement of 50 nanoparticle pairs using SEM, the mean particle size is 337 nm, and the mean interparticle distance is 169 nm.

The noble metal chosen is gold due to its excellent plasmonic properties and resistance to oxidation as compared to silver [20]. The thickness of gold is kept between 20 to 60 nm. For thicknesses greater than 30 nm, the evaporations are done in two steps as the glass transition temperature of the polystyrene mask is low (100 ^{o}C [101]). The substrate is allowed to cool in between sessions. The colloidal mask is removed using Kapton tape removal. Optionally, a solvent (Tylenol) ultrasonication step can be used if necessary. However, the compatibility of solvent ultrasonication with the substrate needs to be kept in mind. It is observed that the quality of the mask also dictates the yield of mask removal, which is above 97% for our samples.

Figure 4.1b-d shows the SEM scans of nanoparticle arrays resulting from the 4:1 IPA and PSL recipe, the DIPGIP recipe, and the DIPGIP plus solvent annealing recipe, respectively. Chapter 3 establishes that the quantitative

mean defect densities are 61%, 20%, and 4%, respectively, for these nanoparticle arrays. Therefore, the significant contributions to defects in the interstitial spaces are due to grain boundaries and evaporation-induced line defects. These figures further validate the resistance of the solvent annealed masks to cracking around point defects.

4.2 Optical Properties

The surface-enhanced Raman enhancement is optimized by placing the sensor plasmon resonance wavelength halfway between the laser excitation wavelength, and the Raman shifted photon wavelength [6]. As such, the first step in optical characterization is to probe and optimize the plasmon resonance wavelength. For most commonly available research Raman instrumentation, the laser excitation wavelengths are set at 532 nm, 633 nm, and 785 nm. Therefore, the preferred ranges for the optimal SERS enhancement can be calculated as shown in Table 4.1. These ranges serve as guidelines for the following sensor design process.

The plasmon resonance wavelength of a nanoparticle array is determined using UV-Vis reflectance spectroscopy [22]. In this technique, the reflectance of a surface is mapped for the incident visible to near-infrared wavelengths. The plasmon resonance condition is ascribed to the global minimum point in the reflectance plot. It is noted that this technique gives a macroscopic picture of the optical response due to the large spot size of the incident beam ($\sim$2 mm). Figure 4.2a shows a generalized cross-section of our sensor, and Figure 4.2b shows the reflectance plots for the optimized nanoparticle arrays as a function of the evaporated metal thickness. The silicon wafers feature a thin native oxide measured at 1.2 to 1.5 nm thick using ellipsometry (Table 4.2). As expected, the plasmon resonance wavelength blue-shifts 1.9 nm for a 1 nm increase in the evaporated metal thickness. However, the resonance wavelengths are outside of the relevant optimal ranges given above.

The resonance wavelength can be shifted by changing the nanoparticle shape, size, or spacing, using material overlayers, or changing the substrate refractive index [4]. The colloidal mask fixes the nanoparticle array geometry, and the material overlayers result in inaccessible hot spots and reduced electromagnetic field intensities. Silicon wafers naturally offer two materials close

to the nanoparticles: silicon dioxide (n = 1.46) and silicon (n = 3.98). Since the penetration depth of plasmon electromagnetic fields is around 5 to 15 nm [45], the nanoparticles "feel" the higher refractive index silicon substrate in the native oxide wafers. A reduction in the substrate refractive index can be induced by growing a thicker oxide. This variation offers a much cheaper and more straightforward process than growing thin films using chemical vapor deposition processes. Figure 4.2c shows the blue-shifted reflectance plots of the nanoparticle arrays on 300 nm wet oxide silicon wafers. The resultant shift of 192 nm places the plasmon resonance proximal to the optimal range for the 532 nm excitation laser. The shift sensitivity also decreases to 0.45 nm for a 1 nm increase in evaporated metal thickness. This resonance shift is expected to be proportional to the oxide thickness until the oxide thickness exceeds the plasmon field penetration depth [45]. Therefore, future work would tune the resonance wavelength into the optimal range for the 633 nm laser excitation wavelengths with oxide thicknesses below 15 nm.

Flexible polymer films that can efficiently swab an arbitrarily shaped target surface for analytes [102] can be used in conjunction with the rigid sensors shown above. Placing a PDMS slab on the sensor surface leads to a resonance red-shift of 52 nm due to refractive index change from 1 (air) to 1.43 (PDMS). This film serves as an excellent capping material with transparency in the visible to near-infrared regimes [49], and chemical inertness [69].

4.3 Surface Enhanced Raman Scattering Properties

Quantitative characterization of the SERS enhancement effect is performed with the non-resonant nucleobase adenine. Adenine is chosen due to its ability to strongly adsorb onto the metal surface, displace the existing atmospheric adsorbents and form a stable complex with the metal atoms [103]. Figure 4.3a shows the molecular sketch labeled with commonly used site assignments. Samples are incubated overnight in a 400 µM neutral pH adenine solution, resulting in uniform molecular layer adsorption on the nanoparticle array. Upon extraction, samples are rigorously washed with DI and blow-dried with nitrogen gas. The SERS spectra of an adenine monolayer (Figure 4.3b) are compared for an optimized nanoparticle array (ONPA), an unoptimized nanoparticle array (UNPA), and a gold film. It is important to

note that adenine has a low Raman cross-section [104] unlike commonly used Raman dyes and thiolated molecules. Therefore, the ONPA shows a high enhancement factor for detecting the characteristic adenine peaks. These molecular peaks with their assignments are listed in Table 4.3. The UNPA has a low signal-to-noise ratio; therefore, only the dominant ring breathing mode (732 cm^{-1}) is definitively detected, while no molecular peaks are observed on the gold film.

The major bands observed at 732, 1239, 1314, 1337 and 1450 cm^{-1} agree well with past experimental studies and density functional theory simulations [105–109]. However, a significant difference is the presence of 1628 and 1672 cm^{-1} bands, which generally have non-detectable intensities in the SERS spectra. These bands are analogous to the non-enhanced Raman bands of 1613, and 1674 cm^{-1} [105]. The wavenumber shifts are expected due to the existence of a charge complex and the resultant chemical enhancement, or possible differences in molecular orientation [105,110]. The adenine molecules are believed to be oriented at a tilted angle on the metal surface with adsorption at N7 and the amine group (N10) sites. As a result, 1239, 1450, and 1672 cm^{-1} bands have significant contributions from the amine group scissoring or rocking vibrations. Additionally, all the major bands except 732 cm^{-1} have a contribution from N7 related stretching vibrations. The discrepancy for bands above 1600 cm^{-1} could be a contribution from the optimized enhancing surface in this thesis. The plasmon resonance wavelength of the nanoparticle array at 567 nm is proximal to the ideal resonance wavelengths of these bands.

The notable out-of-plane vibration modes below 1000 cm^{-1} have weak intensities due to the tilted orientation of the adenine molecule. These bands are not observed due to the strong phononic Raman spectra of the silicon substrates [111] shown in Figure 4.4a. The enhancement of the higher-order acoustic and optical phonon mode can be attributed to the low surface coverage of 7.2% for the nanoparticle array [112] and a higher percentage of incident light interacting with silicon. Near-field enhancement of the phonon modes is ruled out due to the thickness of the silicon oxide (300 nm) exceeding the penetration depth of the plasmon electromagnetic fields.

The SERS enhancement factor captures the magnification of the Raman signal provided by the enhancing surface to a standard. The commonly used

formula [112] is,

$$EF = \frac{I_{sers}}{I_{standard}} \times \frac{N_{standard}}{N_{sers}}, \tag{4.1}$$

where I denotes the normalized peak intensities for the adenine ring breathing mode and N represents the number of excited molecules. The chosen standard is a 20 mM adenine aqueous solution. The resultant peak height at 717 cm^{-1} is attributed to the ring breathing mode [113]. The number of adenine molecules excited in solution is,

$$N_{standard} = c \times N_A \times V, \tag{4.2}$$

where c is the solution concentration, N_A is the Avogadro constant, and V is the confocal volume. The confocal volume is the in-focus volume of the sample that is excited by the incident laser beam using confocal optics [114]. A simplification is used to alleviate the need for direct measurement of the confocal parameters using the $1/e^2$ analysis [112]. The confocal volume is assumed to be cylindrical (Figure 4.4b inset) with the diameter given by the spot size (w) and the height given by the depth of focus or the confocal parameter (L) [14, 115]. The confocal parameter is indirectly measured from the peak intensity curve of the silicon transverse optical phonon mode at 520 cm^{-1} as a function of the substrate displacement in the z direction [14]. This curve is shown in Figure 4.4b. The confocal parameter is measured as the displacement associated with $1/e^2$ of the peak intensity value. The resultant confocal parameter is 7.52 µm for the 100x objective with a numerical aperture (NA) of 0.8. It is noted that the silicon surface is sampled even when the microscope is focused on the oxide surface.

The measured confocal parameter is a conservative estimate of the experimental counterpart [14], which is shown by comparing the simplified confocal volume and the theoretical confocal volume. The simplified confocal volume is given by,

$$V_{est} = w \times L. \tag{4.3}$$

The spot size can be back-calculated by assuming a pseudo-Airy pattern that is typical for high NA confocal objectives [116],

$$w = \frac{1.22 \times L \times NA}{4} = 2.24\ \mu m, \tag{4.4}$$

thereby giving a confocal volume,

$$V_{est} = \pi \times (0.5 \times 2.24 \times 10^{-6})^2 \times 9.16 \times 10^{-6} = 0.036\ pL. \tag{4.5}$$

The theoretical confocal volume is given by [114],

$$V_{th} = \pi^{1.5} \times k \times w^3, \tag{4.6}$$

where k is the ratio of the optical resolution in z to the optical resolution in the x-y plane. In the case of diffraction-limited optics, the lower limit of k can be calculated,

$$k = \frac{2.33 \times n}{NA} = \frac{2.33 \times 1}{0.8} = 2.91, \tag{4.7}$$

where n is the refractive index of 1 for air. Therefore, the lower limit of the confocal volume possible is,

$$V_{th} = \pi^{1.5} \times 2.91 \times (2.24 \times 10^{-6})^3 = 0.18\ pL. \tag{4.8}$$

It is important to note that the spot size measurement indicates a non-perfect optical system. In that case, the value for k should increase, thereby increasing the confocal volume further than the theoretical value [114].

The number of adenine molecules excited on the nanoparticle array surface is,

$$N_{sers} = P \times AF \times w, \tag{4.9}$$

where P is the approximate packing density of adenine, AF is the area factor, and w is the spot size. The packing density is approximated for an adenine monolayer to be 1.07×10^{18} m^{-2} from scanning tunneling microscopy studies [117]. It is noted that the monolayer deposited in solution should be more disordered than the perfect monolayer assembled in vacuum [118]. The area factor for the nanoparticle array is known to be 0.072 [112]. Since the spot size appears in both N_{raman} and N_{sers}, it cancels out in the EF equation.

The calculated EFs are listed in Table 4.4 along with λ_d, which measures the mismatch between the ideal resonance wavelength and the experimentally measured resonance wavelength. The ONPA reaches an EF of 8.95×10^6 with a λ_d of 24 nm. The EF drops for the UNPA to 2.36×10^6 with a λ_d

of 126 nm. Therefore, the maximization of EF requires the careful matching of the resonance wavelength to the excitation wavelength. The presented EFs are comparable to the values published for non-resonant molecules on nanoparticle arrays fabricated by nanosphere lithography [6]. Higher EFs can be unlocked by decreasing the size of the nanoparticles to decrease ohmic losses [5] and using silver instead of gold [22].

Rhodamine 6G (R6G) is a cationic dye molecule frequently employed as a probe for studying SERS systems [84, 119–121]. R6G is a weakly adsorbing molecule; therefore, it allows a comparative study on the accessibility of the hot spots on the metal surface [103, 122]. Additionally, R6G is a good candidate for studying the uniformity of the SERS response due to its large non-resonant Raman cross-section [123] and presence of multiple sharp peaks as compared to one dominant peak for adenine. Figure 4.5 compares the SERS spectra of R6G with adenine on UNPA arrays. R6G molecular layers are adsorbed by soaking samples in 1 µM R6G aqueous solutions for 3 hours. The samples are rigorously washed with DI upon extraction. As expected, the R6G spectra feature more enhanced and sharper peaks as compared to the adenine spectra. The dominant mode peaks at 614, 776, 1187, 1315, 1364, and 1513 cm^{-1} are highlighted. The coefficients of variation (Table 4.5) for all the peak intensities are below 12%, thereby demonstrating good nanoparticle ordering.

4.4 Angle-Resolved Nanosphere Lithography

The nanoparticle arrays studied until now are a result of a single gold evaporation step at normal angles to the substrate. The interparticle gaps in these arrays are intrinsically tied to the nanosphere diameter. This relation can be broken by changing the angles between the metal source and the shadow mask between two or more evaporation steps. This variant technique named angle-resolved nanosphere lithography (ARNSL) allows independent control of the interparticle gap [45]. Figure 4.6 shows the three motifs that result from sequential 20 nm, and 18 nm gold layers evaporated at $\pm 15^o$ on 1 µm colloidal mask. The alignment difference (θ_d) between the grain orientation and the metal influx direction differentiates the motifs. The desired aligned nanoparticles have zero θ_d, misaligned arrays have $\theta_d < 60^o$ and parallel ar-

rays have 60^o θ_d. The hexagonal symmetric mask restricts the misalignment differences to 60^o.

4.5 Flexible Sensors

Flexible SERS sensors are well suited for real-time monitoring functionalities in environmental, defense, manufacturing, and medical applications [102, 124]. A key requirement for flexible sensors is the presence of uniform and large signal enhancement in addition to mechanical flexibility [125]. Nanoparticle arrays fabricated by NSL on soft substrates have been shown as good candidates for such requirements [76,126,127]. Figure 4.7a shows a nanoparticle array fabricated on a PDMS substrate. The colloidal mask structure is detailed previously in Figure 2.7. The insulating nature of PDMS requires the use of environmental SEM. It is seen that the nanoparticle anisotropy is decreased on PDMS as compared to nanoparticles fabricated on silicon [128]. The nanoparticle array is linearly strained using a home-built setup shown in Figure 4.7c. The setup consists of a metallic frame and a sliding block supported on linear guide rails inside the frame. The PDMS sample is clamped between one end of the frame and the sliding block. Tensile strain is applied by a 4-40 screw pushing the sliding block away from the clamp side of the frame. Figure 4.7b shows the broken-symmetry nanoparticle array at 50% substrate strains. The linear relation between substrate strains and the interparticle gap for gold nanoparticles is detailed in past literature [71, 76].

4.6 Methods

Physical Vapor Deposition: Thermal evaporation is performed using a Denton DV-502A thermal evaporator with a custom stage. The purpose-built evaporator setup shown in Figure 4.8 consists of two electrodes with tungsten boats, a shutter, and housing for the substrate and the quartz crystal sensor. The angle between the substrate and the two metal sources are kept at 15^o for ARNSL applications. Gold chips are degreased before loading into the tungsten boats. Gold metal layers are evaporated with manual current control at 0.5-1 nm/s. The chamber pressures are kept at

5×10^{-6} torr. Electron beam evaporation is performed in a Kurt Lesker PVD75 pro-line evaporator. Gold is evaporated at 0.07 nm/s and 1×10^{-6} torr pressures. Evaporated thicknesses are constrained to 30 nm per session to prevent mask degradation due to heating. It is important to note that the polystyrene mask has a low glass transition temperature of 100 ^{o}C [101]. The system is allowed to cool for 5 mins between evaporation sessions.

Scanning Electron Microscopy: SEM and ESEM scanning is performed using an FEI Quanta FEG 450 ESEM with Everhart-Thornley secondary electron detector and 1000 µm gaseous secondary electron detector, respectively. SEM scan parameters are high-vac mode (10^{-6} torr), 10 kV accelerating voltage, 5 mm working distance, 20 µs dwell time, and 3.0 spot size. ESEM scan parameters are 5 torr water vapor pressures, 20 kV accelerating voltage, 10 mm working distance, 40 µs dwell time, and 3.0 spot size. Gap analysis is carried out using Gwyddion and Python scripts. FFT analysis is done using Image J.

UV-Vis Spectroscopy: The reflectance properties of nanoparticle arrays are characterized using a Zeiss Axio Observer D1 microscope with a 100 W halogen variable intensity light source and a UV-Vis (300 to 900 nm) silicon photodiode array spectrometer. A 20x objective with an N.A. of 0.4 is used to focus the light into a $\sim$ 1 mm spot. Evaporated gold films are used as references. The signal is integrated for up to 1 s and averaged over five captures to generate a stable curve.

Ellipsometry: Silicon oxide thicknesses are measured using a Gaertner Scientific Stokes Laser ellipsometer. The system offers plug-and-play functionalities with minimum setup.

Raman Characterization: Adenine and rhodamine 6G are purchased from Sigma Aldrich Inc. Since adenine has poor solubility in room temperature water [129], adenine powder is dissolved in DI kept at 95 ^{o}C with constant stirring. The resultant 20 mM stock solutions are diluted to 400 µM concentrations for sample preparation. Samples are soaked in 400 µM adenine solution or 1 µM R6G solutions for molecular layer adsorption. Samples are rigorously washed with DI and dried with nitrogen gas upon extraction.

SERS properties are studied using a Horiba LabRam HR Raman spectroscopy confocal imaging system equipped with 50 W 532 nm and 35 W 633 nm lasers. Incident laser power is reduced using neutral density filters of varying optical densities. The ONPA sample is probed using 5 mW 532

nm laser light, and the UNPA and the gold film are probed using 8.79 mW 633 nm laser light. All spectra have been normalized for laser power and signal integration times. Confocal objective with 100x mag, 0.8 NA and 1800 g/mm grating are used for all measurements. The calculated spot size is $\sim$ 2.24 µm.

Raman measurements are made on a 20 mM adenine solution for EF determination. Newly prepared adenine solution is poured into fabricated microwells made using cut PDMS films pasted on silicon substrates. The microwells are covered using glass cover slides. Since the adenine solutions have low concentration and adenine has a low Raman cross-section, the full power of the incident lasers is used for Raman signal measurement.

4.7 Figures and Tables

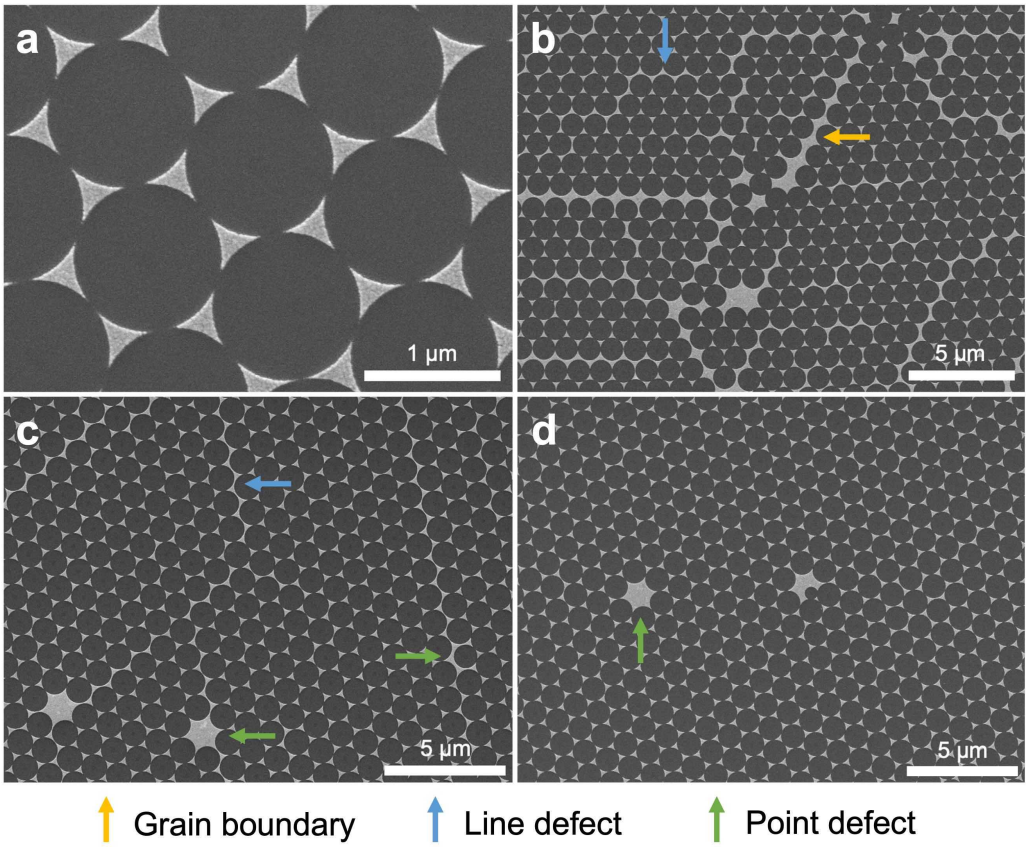

Figure 4.1: (a) Triangular-shaped nanoparticle array, Nanoparticle arrays produced from (b) 4:1 IPA and PSL recipe, (c) DIPGIP recipe, (d) DIPGIP plus solvent annealing recipe.

Table 4.1: Optimal ranges for maximum SERS enhancement. λ_{ex} are the commonly available Raman excitation wavelengths. λ_{sh} are the expected shifted wavelength ranges for the relevant SERS molecular bands. λ_{op} are the calculated optimal ranges.

λ_{ex}	λ_{sh}(600 - 1600 cm^{-1})	λ_{op}
532 nm	550 - 582 nm	541 - 557 nm
633 nm	658 - 704 nm	646 - 669 nm
785 nm	824 - 898 nm	805 - 842 nm

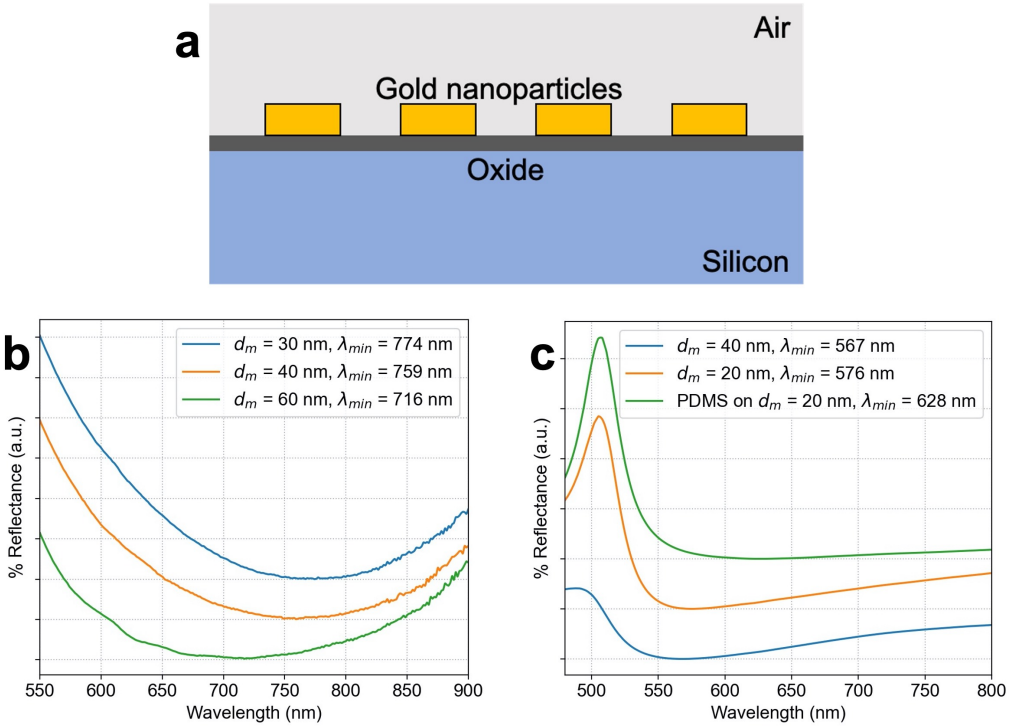

Figure 4.2: (a) Generalized cross-section of the sensor surface, (b) Reflectance plots of nanoparticle arrays on native oxide silicon wafers, (c) Reflectance plots of nanoparticle arrays on 300 nm wet oxide silicon wafers. d_m is the thickness of the evaporated gold measured by the crystal monitor.

Table 4.2: Ellipsometry measurement data of silicon oxide thicknesses for wafer 1 (100 mm, native oxide, n-type) and wafer 2 (50 mm, native oxide, p-type). Each wafer is measured at four random locations.

Wafer No.	ψ	Δ	Oxide thickness (nm)
1	11.023	174.956	1.444
1	11.009	174.972	1.439
1	10.988	174.831	1.487
1	10.983	174.916	1.458
2	10.982	175.471	1.267
2	10.990	175.479	1.264
2	10.991	175.688	1.192
2	10.998	175.479	1.264

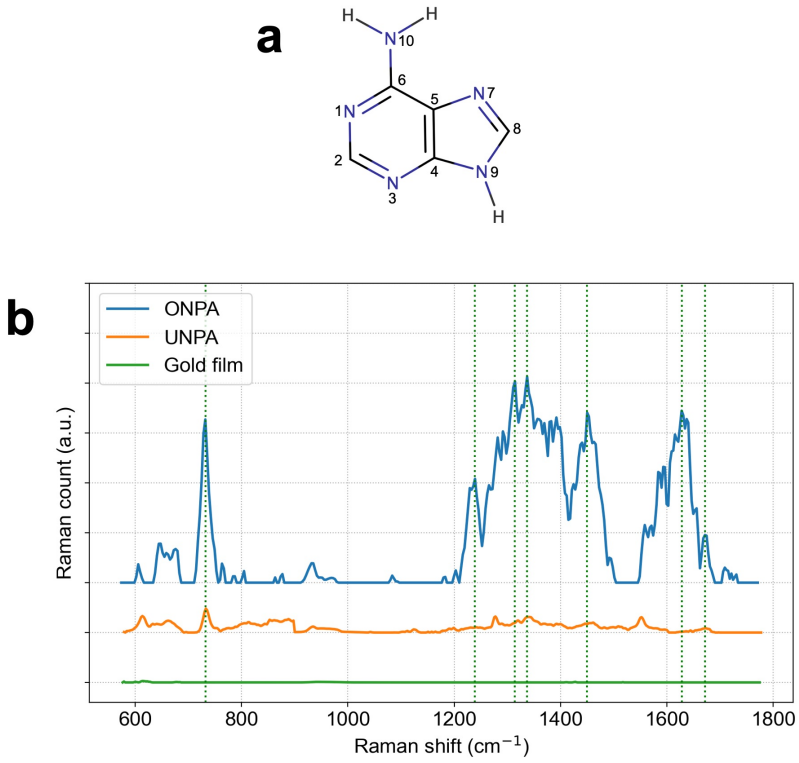

Figure 4.3: (a) Molecular sketch of adenine labled with site assignments, (b) SERS spectra of an adenine monolayer on an optimized nanoparticle array (ONPA), an unoptimized nanoparticle array (UNPA), and a gold film.

Table 4.3: Adenine molecular bands observed in Figure 4.3b. ^{b} = bending, ^{r} = rocking, ^{s} = stretching and ^{sc} = scissoring.

Shift (cm^{-1})	Assignment [105], [106], [109]
732	Ring breathing mode
1239	(C5N7, N1C2, C2N3)^{s}, $NH_2{}^{r}$
1314	(C2N3, C5N7, N1C2, C5C6)^{s}
1337	(N1C2, C5N7)^{s}, (C2H, C8H)^{b}
1450	(N7C8, N1C6)^{s}, C8H^{b}, $NH_2{}^{sc}$
1628	(N3C4, N1C6, C5N7, N7C8)^{s}, N9H^{b}
1672	(C6N10, C5C6)^{s}, $NH_2{}^{sc}$

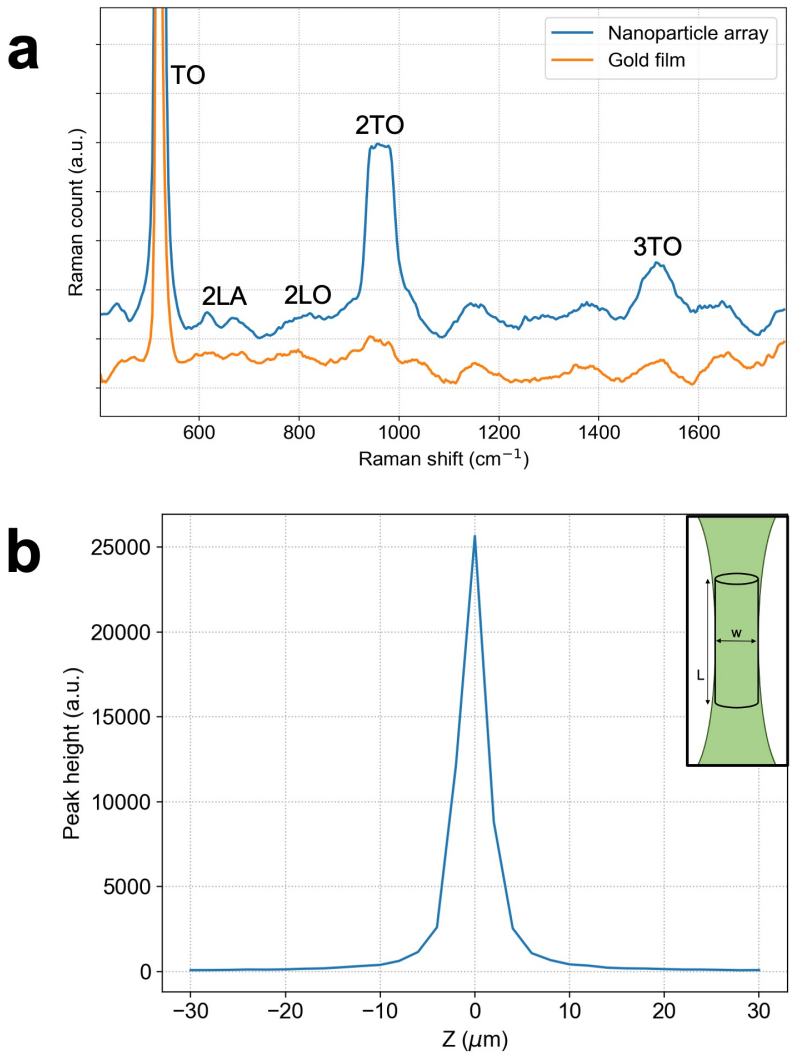

Figure 4.4: (a) Background Raman spectra without presence of an adenine monolayer, (b) Peak height of silicon transverse optical phonon band at 520 cm^{-1} as a function of height displacement.

Table 4.4: Enhancement factors (EF) for nanoparticle arrays with different plasmon resonance wavelengths (λ_{min}). Here, λ_{ex} = excitation wavelength, $\lambda_{opt-732}$ = optimal resonance wavelength for 732 cm^{-1}, and, λ_d = λ_{min} - $\lambda_{opt-732}$.

λ_{ex}	$\lambda_{opt-732}$	λ_{min}	λ_d	EF
633 nm	649 nm	774 nm	126 nm	2.36 x 10^6
633 nm	649 nm	716 nm	68 nm	3.73 x 10^6
532 nm	543 nm	567 nm	24 nm	8.95 x 10^6

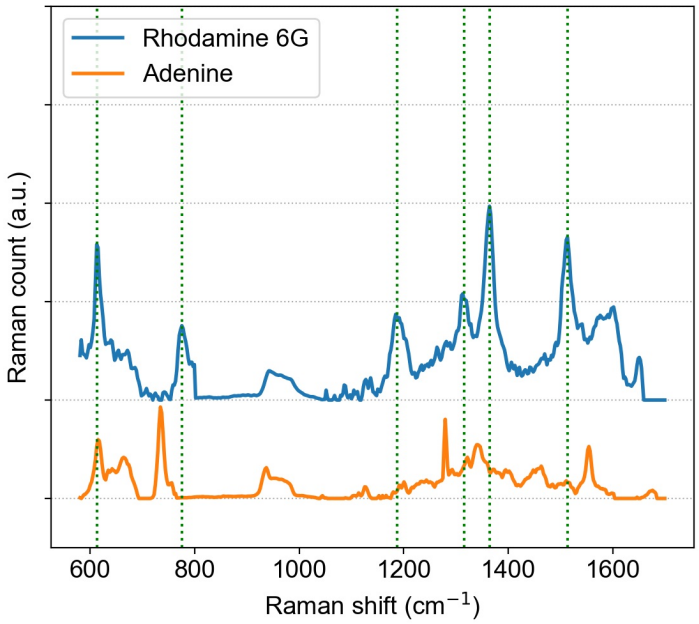

Figure 4.5: Comparison of the spectras between the high Raman cross-section dye rhodamine 6G with the low Raman cross-section nucleobase adenine. Monolayers of the molecules are adsorbed on two UNPA samples. The samples are characterized with 633 nm 8.79 mW laser with a 100x objective (NA = 0.8).

Table 4.5: Percentage coefficient of variation (CV) for the dominant bands of Rhodamine 6G for 10 random spots.

Band (cm^{-1})	CV (%)
614	5.79
776	6.90
1187	9.22
1315	11.44
1364	10.29
1513	11.81

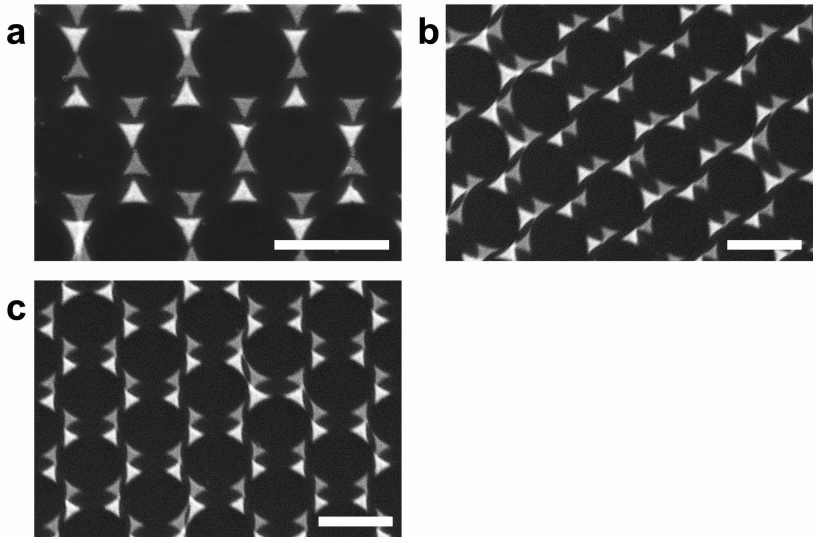

Figure 4.6: (a) Aligned nanoparticle array, (b) Misaligned nanoparticle array, (c) Parallel nanoparticle array. All scale bars are 1 µm.

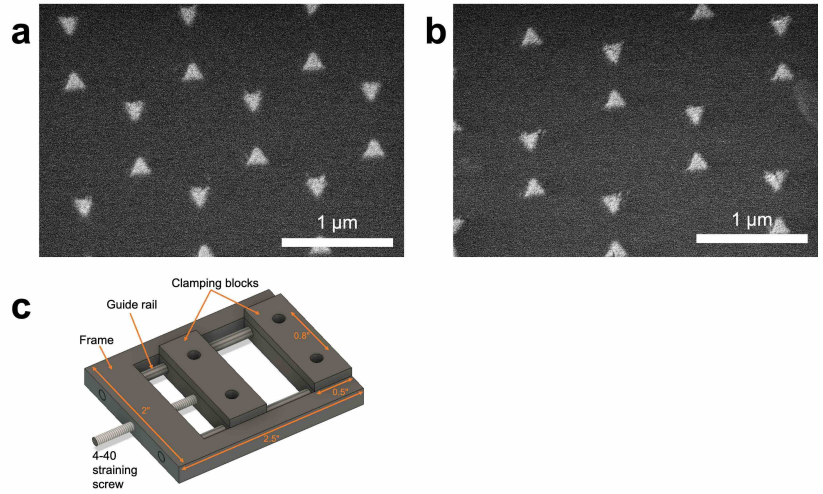

Figure 4.7: (a) Nanoparticle array on PDMS substrate, (b) Nanoparticle array with 50% substrate strain, (c) Sketch of the home-built linear strain device.

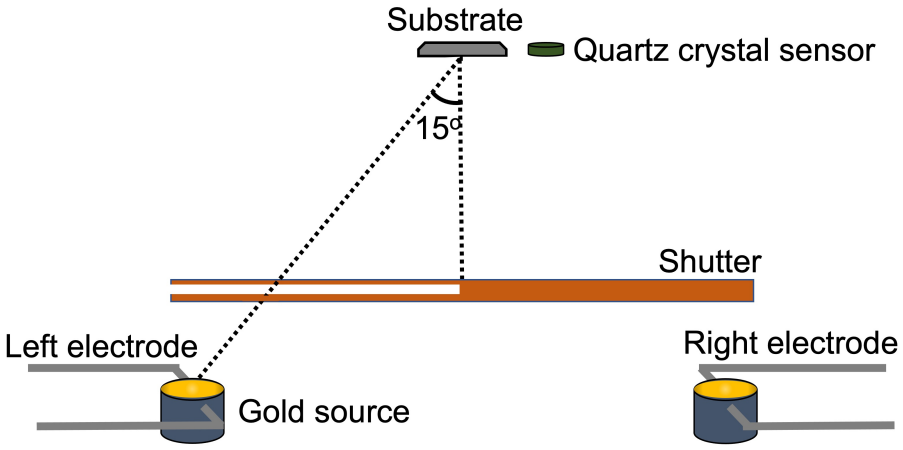

Figure 4.8: Thermal evaporator setup.

CHAPTER 5

FUTURE WORK

Reliable fabrication of highly dense arrays of sub-10 nm gap dimer particles arrays remains an unsolved challenge. Top-down literature solutions typically rely on careful addition of atomic layers through atomic layer deposition [130] or specialized electron beam lithography processes [12, 131]. However, not many solutions are present for the low-cost and low complexity realization of this aim. For this purpose, a simple process for large-area low-defect single-crystal colloidal masks is developed. The implementation of the optimized masks in an ARNSL process realizes the thesis aim. Here, the critical challenges that require further study are detailed.

5.1 Colloidal Mask

The colloidal mask self-assembly relies on the convective flow from the IPA evaporation to drive the colloidal spheres to the air-water interface. PG reduces the hydrophobic-hydrophobic interactions between the spheres and allows easier reorientation of aggregates. The elevated hydrophilicity results in the increased stability of the spheres in the bulk of the DI layer [55], which necessitates draining of the DI layer. Another issue with the presented technique is the requirement for hydrophilicity of the used substrates. Therefore, it is incompatible with hydrophobic substrates like PDMS. These issues can be quickly and scalably addressed in the ring confinement setup shown in Figure 2.6. The design contains an outlet pipe that creates a horizontal drain current, which eliminates the spheres entering the bulk volume of the water. The ring confinement secures the unoptimized colloidal crystal layer during this process. Additionally, the ring confinement allows for careful placement and deposition of the colloidal mask on substrates with any levels of hydrophobicity. It is noted that the colloidal crystal optimization pro-

cess is not well understood. The increased complexity from the combination of the surface depression due to the ring, the anisotropic geometries of the trough, and the interaction of energy sources with the setup require further experimentation. The energy source can be simplified to a surface wave generator in such complex cases. Surface waves are periodically generated by submerging, withdrawing a polymer block in and out from the water.

Room temperature air drying of colloidal mask layers results in a significant amount of evaporation-induced crystal cracking. Solvent annealing is presented as an effective solution in this thesis. However, achieving uniform solvent vapor over large-area masks requires significant vapor flow and process simulation. A low-cost alternative is a sintering approach [132] that leverages the ability of PG to keep the crystal wet.

The large quasi-single crystals demonstrate a relative crystal twist variation of less than 0.5^o per mm. The achieved crystal quality is sufficient for most research applications. Single crystals are shown in Figure 3.11b result from the enforcement of a glocal boundary condition using a hydrophobic Kapton tape template. This idea can be extended to hexagonal template rings placed on air-water interfaces. Preliminary self-assemblies with laser-cut hexagonal acrylic rings shown in Figure 5.1 demonstrate positive results. To our knowledge, this work has not been done in the literature.

5.2 Nanoparticle Array

The application of ARNSL with the optimized masks needs to be characterized. This study will determine the relationship between the substrate angle and the achieved interparticle gap. The thesis has established the direct link between the colloidal crystal imperfection and the nanoparticle array defect density. Lower diameter CV nanospheres should be purchased or fabricated in the lab to achieve lower standard deviations (SD). Currently, a 3.56% areal defect density due to the miscoordinated spheres is detected. The precursor nanosphere diameter CV is 3%. Hence, the resultant nanoparticle height SD is 49 nm, and the interparticle gap SD is 14 nm. Additionally, a theoretical simulation framework using finite domain time difference needs to be established [12]. This will ensure faster design to fabricated sensor times and deepen understanding of the achieved electromagnetic phenomena.

Further study will establish the relation between the interparticle gap and the LSPR wavelength red-shift associated with interparticle coupling. The theoretical limit of the interparticle gap and the associated SERS enhancement factor can be established. Alternative routes of achieving precise interparticle gaps using atomic layers [130] can also be explored.

5.3 Miscellaneous Projects

Our NSL study provided the freedom and previledge to participate in various device fabrication projects. Preliminary work from these projects is shown in Figures 5.2 to 5.6. These Figures each offer a new avenue for further research.

5.4 Figures

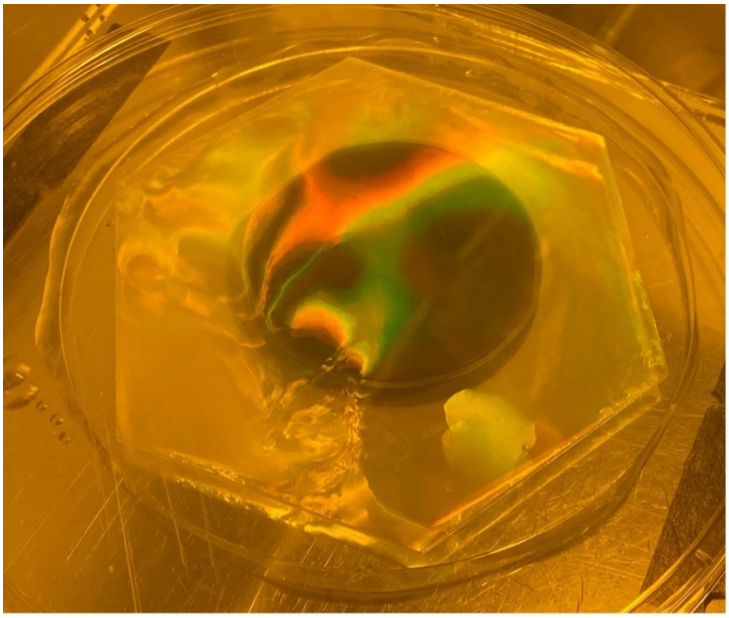

Figure 5.1: Colloidal crystal assembled on the curved air-water interface of a DI thin film with a polymer hexagonal ring confinement. The target 100 mm diameter silicon wafer is positioned inside the DI thin film. Single orientation enforcement is qualitatively assessed from the straight diffraction patterns.

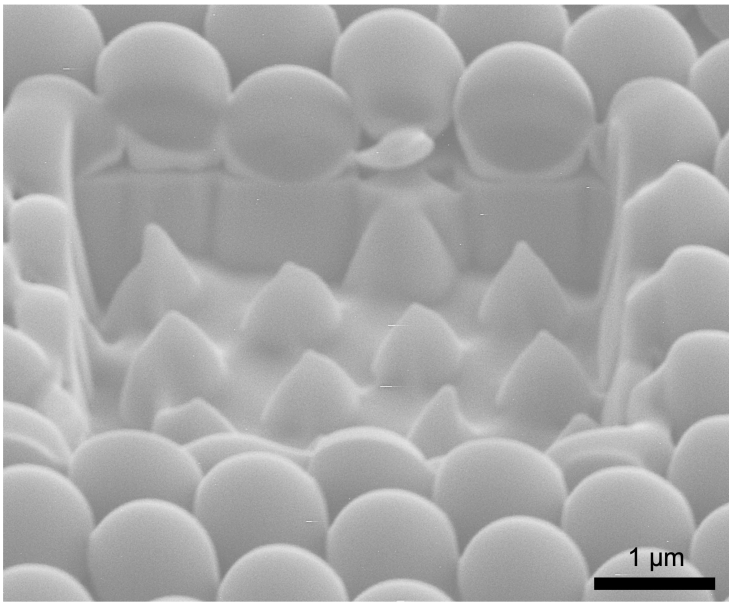

Figure 5.2: Silicon tip array [133] fabricated by galium ion beam milling at 1000 pA for 10 s. Ion beam milling etches both the mask and the substrate resulting in a pointed tip shape due to the undercut beneath the mask. (Courtesy: ECEB Nanofabrication Lab.)

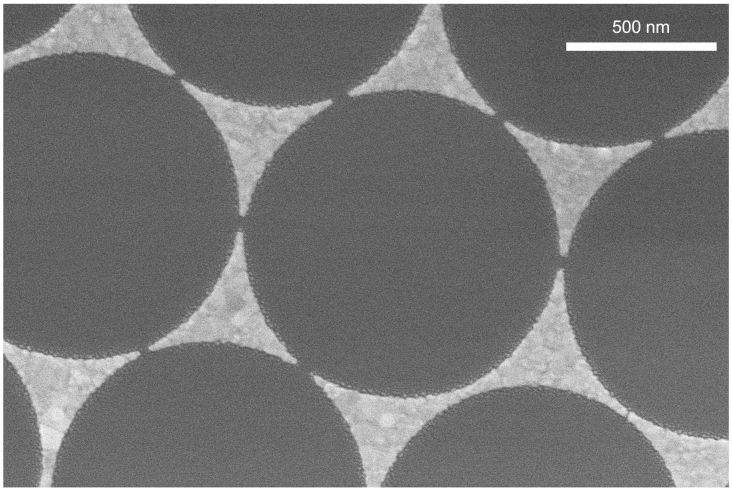

Figure 5.3: Nanoparticles fabricated using oxygen plasma etched nanosphere masks [134]. The interparticle gap mean is reduced from 169 nm (untreated) to 35 nm. The uniformity of the etching process is dependent on the density of point defects. The mask gets etched more at the defect sites due to the higher available surface area. Oxygen plasma descum is performed for 5 mins at 250 W using a Diener Tetra-30 Plasma System.

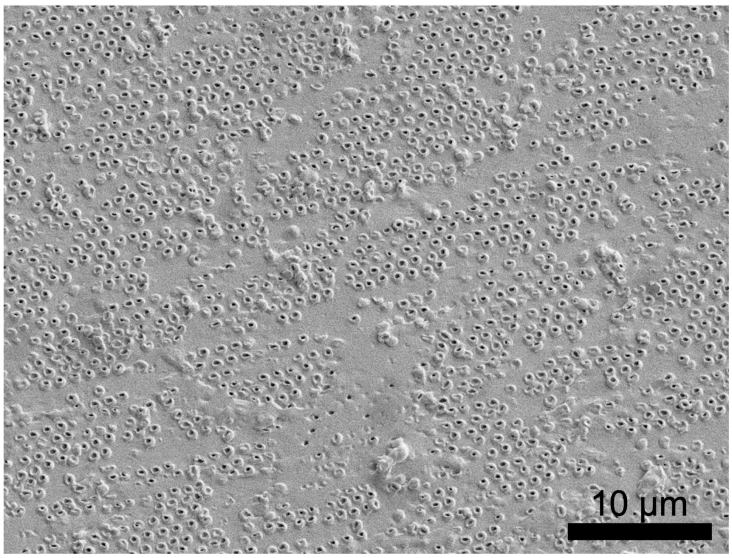

Figure 5.4: Patterned PDMS layer with suction cups [120]. A colloidal mask layer is UV thinned and annealed to achieve periodic non-close packed polystyrene hemispheres. The PDMS layer is spin-coated and cured on the hemispheres. Upon extraction, the polystyrene hemispheres are dissolved using a polar solvent. (Courtesy: Jihong Min, ECEB Nanofabrication Lab.)

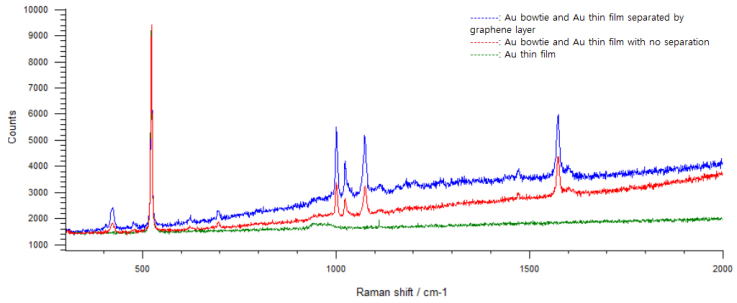

Figure 5.5: SERS spectra of thiophenol on a gold bowties/graphene/gold layer sandwich, a gold bowtie/gold layer sandwich, and a gold layer. Higher enhancement is expected for the first system due to the coupling effect between the gold bowtie and the gold layer and the chemical enhancement provided by graphene [135]. All evaporated gold layers are 20 nm thick. (Courtesy: Eric Wynne.)

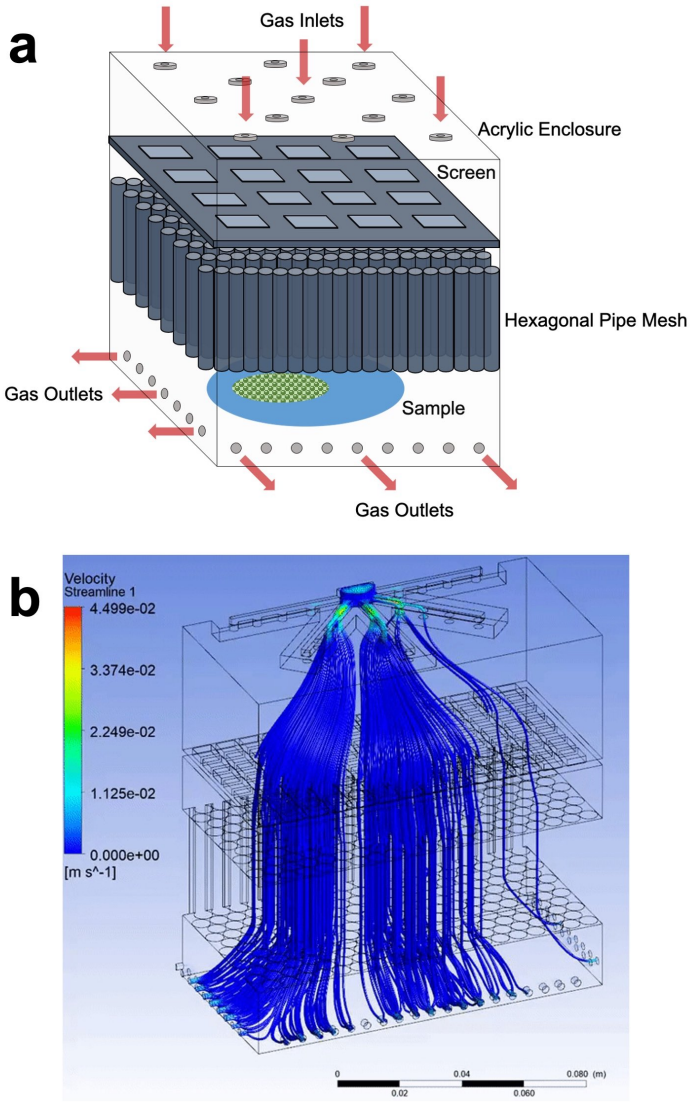

Figure 5.6: (a) Purpose-built chamber for solvent annealing of polystyrene masks, (b) CFD simulation of solvent vapor flow through an annealing half cell. The annealing chamber contains a screen and a hexagonal tube mesh to induce laminar vertical flow. (Courtesy: Martin Evtimov.)

REFERENCES

[1] D. J. Gardiner, "Introduction to Raman scattering," in *Practical Raman Spectroscopy*. Springer, 1989, pp. 1–12.

[2] K. A. Willets and R. P. Van Duyne, "Localized surface plasmon resonance spectroscopy and sensing," *Annu. Rev. Phys. Chem.*, vol. 58, pp. 267–297, 2007.

[3] P. Avouris, D. B. Farmer, M. Freitag, Y. Li, T. Low, H. Yan, and H. Wang, "Graphene plasmons: Properties and applications," in *Active Photonic Materials VI*, 2014, vol. 9162, p. 91620V.

[4] C. L. Haynes and R. P. Van Duyne, "Nanosphere lithography: A versatile nanofabrication tool for studies of size-dependent nanoparticle optics," *The Journal of Physical Chemistry B*, vol. 105.24, pp. 5599–5611, 2001.

[5] E. Hao and G. C. Schatz, "Electromagnetic fields around silver nanoparticles and dimers," *The Journal of Chemical Physics*, vol. 120.1, pp. 357–366, 2004.

[6] X. Zhang, C. R. Yonzon, M. A. Young, D. A. Stuart, and R. P. Van Duyne, "Surface-enhanced Raman spectroscopy biosensors: Excitation spectroscopy for optimisation of substrates fabricated by nanosphere lithography," in *IEE Proceedings-Nanobiotechnology*, vol. 152, no. 6. IET, 2005, pp. 195–206.

[7] J. Theiss, P. Pavaskar, P. M. Echternach, R. E. Muller, and S. B. Cronin, "Plasmonic nanoparticle arrays with nanometer separation for high-performance SERS substrates," *Nano Letters*, vol. 10, no. 8, pp. 2749–2754, 2010.

[8] N. A. Hatab, C. H. Hsueh, A. L. Gaddis, S. T. Retterer, J. H. Li, G. Eres, Z. Zhang, and B. Gu, "Free-standing optical gold bowtie nanoantenna with variable gap size for enhanced Raman spectroscopy," *Nano Letters*, vol. 10, no. 12, pp. 4952–4955, 2010.

[9] C. Zong, M. Xu, L. J. Xu, T. Wei, X. Ma, X. S. Zheng, R. Hu, and B. Ren, "Surface-enhanced Raman spectroscopy for bioanalysis: Reliability and challenges," *Chemical Reviews*, vol. 118, no. 10, pp. 4946–4980, 2018.

[10] K. C. Bantz, A. F. Meyer, N. J. Wittenberg, H. Im, Özge Kurtuluş, S. H. Lee, N. C. Lindquist, S. H. Oh, and C. L. Haynes, "Recent progress in SERS biosensing," *Physical Chemistry Chemical Physics*, vol. 13, no. 24, pp. 11 551–11 567, 2011.

[11] S. Dodson, M. Haggui, R. Bachelot, J. Plain, S. Li, and Q. Xiong, "Optimizing electromagnetic hotspots in plasmonic bowtie nanoantennae," *The Journal of Physical Chemistry Letters*, vol. 4, no. 3, pp. 496–501, 2013.

[12] W. Zhu, M. G. Banaee, D. Wang, Y. Chu, and K. B. Crozier, "Lithographically fabricated optical antennas with gaps well below 10 nm," *Small*, vol. 7, no. 13, pp. 1761–1766, 2011.

[13] H. Kollmann, X. Piao, M. Esmann, S. Becker, D. Hou, C. Huynh, L. Kautschor, G. Bosker, H. Vieker, A. Beyer, and A. Golzhauser, "Toward plasmonics with nanometer precision: Nonlinear optics of helium-ion milled gold nanoantennas," *Nano Letters*, vol. 14.8, pp. 4778–4784, 2014.

[14] X. Yao, S. Jiang, S. Luo, B. W. Liu, T. X. Huang, S. Hu, J. Zhu, X. Wang, and B. Ren, "Uniform periodic bowtie SERS substrate with narrow nanogaps obtained by monitored pulsed electrodeposition," *ACS Applied Materials & Interfaces*, vol. 12.32, pp. 36 505–36 512, 2020.

[15] W. D. Li, F. Ding, J. Hu, and S. Y. Chou, "Three-dimensional cavity nanoantenna coupled plasmonic nanodots for ultrahigh and uniform surface-enhanced Raman scattering over large area," *Optics Express*, vol. 19, no. 5, pp. 3925–3936, 2011.

[16] S. K. Srivastava, A. Li, S. Li, and I. Abdulhalim, "Optimal interparticle gap for ultrahigh field enhancement by LSP excitation via ESPs and confirmation using SERS," *The Journal of Physical Chemistry C*, vol. 120, no. 50, pp. 28 735–28 742, 2016.

[17] L. Golubewa, R. Karpicz, I. Matulaitiene, A. Selskis, D. Rutkauskas, A. Pushkarchuk, T. Khlopina, D. Michels, D. Lyakhov, T. Kulahava et al., "Surface-enhanced Raman spectroscopy of organic molecules and living cells with gold-plated black silicon," *ACS Applied Materials & Interfaces*, vol. 12, no. 45, pp. 50 971–50 984, 2020.

[18] H. Tian, H. Li, and Y. Fang, "Binary thiol-capped gold nanoparticle monolayer films for quantitative surface-enhanced Raman scattering analysis," *ACS Applied Materials & Interfaces*, vol. 11, no. 17, pp. 16 207–16 213, 2019.

[19] W. J. Cho, Y. Kim, and J. K. Kim, "Ultrahigh-density array of silver nanoclusters for SERS substrate with high sensitivity and excellent reproducibility," *ACS Nano*, vol. 6, no. 1, pp. 249–255, 2012.

[20] C. J. C. Wu, Hsin Yu and B. T. Cunningham, "Plasmonic nanogap-enhanced Raman scattering using a resonant nanodome array," *Small*, vol. 8.18, pp. 2878–2885, 2012.

[21] D. Wang, W. Zhu, M. D. Best, J. P. Camden, and K. B. Crozier, "Wafer-scale metasurface for total power absorption, local field enhancement and single molecule Raman spectroscopy," *Scientific Reports*, vol. 3, no. 1, pp. 1–6, 2013.

[22] N. G. Greeneltch, M. G. Blaber, A. I. Henry, G. C. Schatz, and R. P. Van Duyne, "Immobilized nanorod assemblies: Fabrication and understanding of large area surface-enhanced Raman spectroscopy substrates," *Analytical Chemistry*, vol. 85.4, pp. 2297–2303, 2013.

[23] J. Long, H. Yi, H. Li, Z. Lei, and T. Yang, "Reproducible ultrahigh SERS enhancement in single deterministic hotspots using nanosphere-plane antennas under radially polarized excitation," *Scientific Reports*, vol. 6, no. 1, pp. 1–8, 2016.

[24] Y. H. Lai, S. W. Chen, M. Hayashi, Y. J. Shiu, C. C. Huang, W.-T. Chuang, C. J. Su, H. C. Jeng, J. W. Chang, Y. C. Lee, and A. C. Su, "Mesostructured arrays of nanometer-spaced gold nanoparticles for ultrahigh number density of SERS hot spots," *Advanced Functional Materials*, vol. 24, no. 17, pp. 2544–2552, 2014.

[25] R. Xu, R. Li, L. Jia, Z. Zheng, and T. Zhou, "An efficient strategy to prepare ultra-high sensitivity SERS-active substrate based on laser-induced selective metallization of polymers," *ACS Sustainable Chemistry & Engineering*, vol. 9, no. 14, pp. 5038–5049, 2021.

[26] H. Liu, L. Zhang, X. Lang, Y. Yamaguchi, H. Iwasaki, Y. Inouye, Q. Xue, and M. Chen, "Single molecule detection from a large-scale SERS-active Au 79 Ag 21 substrate," *Scientific Reports*, vol. 1, no. 1, pp. 1–5, 2011.

[27] J. Tang, H. Guo, M. Chen, J. Yang, D. Tsoukalas, B. Zhang, J. Liu, C. Xue, and W. Zhang, "Wrinkled Ag nanostructured gratings towards single molecule detection by ultrahigh surface Raman scattering enhancement," *Sensors and Actuators B: Chemical*, vol. 218, pp. 145–151, 2015.

[28] K. Y. Loh and X. Liu, "Gapping into ultrahigh surface-enhanced Raman scattering amplification," *ACS Cent. Sci.*, vol. 4.2, pp. 137–139, 2018.

[29] R. Pilot, R. Signorini, C. Durante, L. Orian, M. Bhamidipati, and L. Fabris, "A review on surface-enhanced Raman scattering," *Biosensors*, vol. 9, no. 2, p. 57, 2019.

[30] P. Kuhler, E. M. Roller, R. Schreiber, T. Liedl, T. Lohmuller, and J. Feldmann, "Plasmonic DNA-origami nanoantennas for surface-enhanced Raman spectroscopy," *Nano Letters*, vol. 14, no. 5, pp. 2914–2919, 2014.

[31] W. J. Cho, Y. Kim, and J. K. Kim, "Ultrahigh-density array of silver nanoclusters for SERS substrate with high sensitivity and excellent reproducibility," *ACS Nano*, vol. 6, no. 1, pp. 249–255, 2012.

[32] J. Li, T. S. Deng, X. Liu, J. A. Dolan, N. F. Scherer, and P. F. Nealey, "Hierarchical assembly of plasmonic nanoparticle heterodimer arrays with tunable sub-5 nm nanogaps," *Nano Letters*, vol. 19, no. 7, pp. 4314–4320, 2019.

[33] J. M. Nam, J. W. Oh, H. Lee, and Y. D. Suh, "Plasmonic nanogap-enhanced Raman scattering with nanoparticles," *Accounts of Chemical Research*, vol. 49, no. 12, pp. 2746–2755, 2016.

[34] X. Zhu, W. Wang, W. Yan, M. B. Larsen, P. Bøggild, T. G. Pedersen, S. Xiao, J. Zi, and N. A. Mortensen, "Plasmon–phonon coupling in large-area graphene dot and antidot arrays fabricated by nanosphere lithography," *Nano Letters*, vol. 14, no. 5, pp. 2907–2913, 2014.

[35] J. Grandidier, D. M. Callahan, J. N. Munday, and H. A. Atwater, "Light absorption enhancement in thin-film solar cells using whispering gallery modes in dielectric nanospheres," *Advanced Materials*, vol. 23, no. 10, pp. 1272–1276, 2011.

[36] P. Moitra, B. A. Slovick, W. Li, I. I. Kravchencko, D. P. Briggs, S. Krishnamurthy, and J. Valentine, "Large-scale all-dielectric metamaterial perfect reflectors," *ACS Photonics*, vol. 2, no. 6, pp. 692–698, 2015.

[37] A. R. Madaria, M. Yao, C. Chi, N. Huang, C. Lin, R. Li, M. L. Povinelli, P. D. Dapkus, and C. Zhou, "Toward optimized light utilization in nanowire arrays using scalable nanosphere lithography and selected area growth," *Nano Letters*, vol. 12, no. 6, pp. 2839–2845, 2012.

[38] L. Ji, Y. F. Chang, B. Fowler, Y. C. Chen, T. M. Tsai, K. C. Chang, M. C. Chen, T. C. Chang, S. M. Sze, E. T. Yu et al., "Integrated one diode–one resistor architecture in nanopillar SiOx resistive switching memory by nanosphere lithography," *Nano Letters*, vol. 14, no. 2, pp. 813–818, 2014.

[39] Y. H. Ho, K. Y. Chen, S. W. Liu, Y. T. Chang, D. W. Huang, and P. K. Wei, "Transparent and conductive metallic electrodes fabricated by using nanosphere lithography," *Organic Electronics*, vol. 12, no. 6, pp. 961–965, 2011.

[40] L. Y. Chen, Y. Y. Huang, C.-H. Chang, Y. H. Sun, Y. W. Cheng, M. Y. Ke, C. P. Chen, and J. Huang, "High performance InGaN/GaN nanorod light emitting diode arrays fabricated by nanosphere lithography and chemical mechanical polishing processes," *Optics Express*, vol. 18, no. 8, pp. 7664–7669, 2010.

[41] A. Purwidyantri, C. H. Chen, B. J. Hwang, J. D. Luo, C. C. Chiou, Y. C. Tian, C. Y. Lin, C. H. Cheng, and C. S. Lai, "Spin-coated Au-nanohole arrays engineered by nanosphere lithography for a Staphylococcus Aureus 16s rRNA electrochemical sensor," *Biosensors and Bioelectronics*, vol. 77, pp. 1086–1094, 2016.

[42] M. Gao, M. Cho, H. J. Han, Y. S. Jung, and I. Park, "Palladium-decorated silicon nanomesh fabricated by nanosphere lithography for high performance, room temperature hydrogen sensing," *Small*, vol. 14, no. 10, p. 1703691, 2018.

[43] D. Wang, A. Zhao, L. Li, Q. He, H. Guo, H. Sun, and Q. Gao, "Bioinspired ribbed hair arrays with robust superhydrophobicity fabricated by micro/nanosphere lithography and plasma etching," *RSC Advances*, vol. 5, no. 117, pp. 96 404–96 411, 2015.

[44] J. A. Rivera, T. C. Galvin, A. W. Steinforth, and J. G. Eden, "Fractal modes and multi-beam generation from hybrid microlaser resonators," *Nature Communications*, vol. 9, no. 1, pp. 1–8, 2018.

[45] A. J. Haes, S. Zou, G. C. Schatz, and R. P. Van Duyne, "A nanoscale optical biosensor: The long range distance dependence of the localized surface plasmon resonance of noble metal nanoparticles," *The Journal of Physical Chemistry B*, vol. 108, no. 1, pp. 109–116, 2004.

[46] C. L. Haynes and R. P. Van Duyne, "Dichroic optical properties of extended nanostructures fabricated using angle-resolved nanosphere lithography," *Nano Letters*, vol. 3, no. 7, pp. 939–943, 2003.

[47] C. L. Haynes, A. D. McFarland, M. T. Smith, J. C. Hulteen, and R. P. Van Duyne, "Angle-resolved nanosphere lithography: Manipulation of nanoparticle size, shape, and interparticle spacing," *The Journal of Physical Chemistry B*, vol. 106, no. 8, pp. 1898–1902, 2002.

[48] C. Garcia Nunez, W. T. Navaraj, F. Liu, D. Shakthivel, and R. Dahiya, "Large-area self-assembly of silica microspheres/nanospheres by temperature-assisted dip-coating," *ACS Applied Materials & Interfaces*, vol. 10, no. 3, pp. 3058–3068, 2018.

[49] A. Zahid, B. Dai, R. Hong, and D. Zhang, "Optical properties study of silicone polymer PDMS substrate surfaces modified by plasma treatment," *Materials Research Express*, vol. 4.10, p. 105301, 2017.

[50] Y. He, B. Zhu, X. Zeng, R. Yang, X. Lv, and W. Yuan, "Fabrication of large-area, close-packed, monolayer colloidal crystals via a hybrid method of spin coating and peeling-draining," *Thin Solid Films*, vol. 639, pp. 98–106, 2017.

[51] J. Sun, C. J. Tang, P. Zhan, Z. l. Han, Z. S. Cao, and Z. L. Wang, "Fabrication of centimeter-sized single-domain two-dimensional colloidal crystals in a wedge-shaped cell under capillary forces," *Langmuir*, vol. 26, no. 11, pp. 7859–7864, 2010.

[52] R. Ye, Y. H. Ye, Z. Zhou, and H. Xu, "Gravity-assisted convective assembly of centimeter-sized uniform two-dimensional colloidal crystals," *Langmuir*, vol. 29, no. 6, pp. 1796–1801, 2013.

[53] F. Bayat, P. Chaghamirzaei, A. Nikniazi, S. Ahmadi-Kandjani, M.-R. Rashidi, and H. Tajalli, "Optimizing the concentration of colloidal suspensions in convective assembly of centimeter-sized uniform monolayer colloidal crystals," *Applied Surface Science*, vol. 434, pp. 898–904, 2018.

[54] K. Shinotsuka, Y. Kajita, K. Hongo, and Y. Hatta, "Crystal perfection of particle monolayer at the air–water interface," *Langmuir*, vol. 31, no. 42, pp. 11 452–11 457, 2015.

[55] X. Meng and D. Qiu, "Gas-flow-induced reorientation to centimeter-sized two-dimensional colloidal single crystal of polystyrene particle," *Langmuir*, vol. 30, no. 11, pp. 3019–3023, 2014.

[56] V. Lotito and T. Zambelli, "Self-assembly of single-sized and binary colloidal particles at air/water interface by surface confinement and water discharge," *Langmuir*, vol. 32, no. 37, pp. 9582–9590, 2016.

[57] J. T. Zhang, L. Wang, D. N. Lamont, S. S. Velankar, and S. A. Asher, "Fabrication of large-area two-dimensional colloidal crystals," *Angewandte Chemie*, vol. 124, no. 25, pp. 6221–6224, 2012.

[58] P. Moitra, B. A. Slovick, W. Li, I. I. Kravchencko, D. P. Briggs, S. Krishnamurthy, and J. Valentine, "Large-scale all-dielectric metamaterial perfect reflectors," *ACS Photonics*, vol. 2, no. 6, pp. 692–698, 2015.

[59] G. Cossio and E. T. Yu, "Zeta potential dependent self-assembly for very large area nanosphere lithography," *Nano Letters*, vol. 20, no. 7, pp. 5090–5096, 2020.

[60] Q. Wei and X. Wu, "Grain boundary dynamics under mechanical annealing in two-dimensional colloids," *Physical Review E*, vol. 70, no. 2, p. 020401, 2004.

[61] Z. Lu and M. Zhou, "Fabrication of large scale two-dimensional colloidal crystal of polystyrene particles by an interfacial self-ordering process," *Journal of Colloid and Interface Science*, vol. 361, no. 2, pp. 429–435, 2011.

[62] J. Yu, C. Geng, L. Zheng, Z. Ma, T. Tan, X. Wang, Q. Yan, and D. Shen, "Preparation of high-quality colloidal mask for nanosphere lithography by a combination of air/water interface self-assembly and solvent vapor annealing," *Langmuir*, vol. 28.34, pp. 12 681–12 689, 2012.

[63] K. Ariga, Y. Yamauchi, T. Mori, and J. P. Hill, "25th anniversary article: What can be done with the Langmuir-Blodgett method? Recent developments and its critical role in materials science," *Advanced Materials*, vol. 25, no. 45, pp. 6477–6512, 2013.

[64] M. Shishido and D. Kitagawa, "Preparation of ordered monoparticulate film from colloidal solutions on the surface of water and continuous transcription of film to substrate," *Colloids and Surfaces A: Physicochemical and Engineering Aspects*, vol. 311.1-3, pp. 32–41, 2007.

[65] P. A. Kralchevsky and K. Nagayama, "Capillary forces between colloidal particles," *Langmuir*, vol. 10, no. 1, pp. 23–36, 1994.

[66] D. Chandler, "Two faces of water," *Nature*, vol. 417.6888, p. 491, 2002.

[67] B. Li, I. Avrutsky, Y. Zhao, and G. Mao, "Statistical study of two-dimensional colloidal crystals based on microscopic images and optical diffraction," *Colloids and Surfaces A: Physicochemical and Engineering Aspects*, vol. 174, no. 1-2, pp. 113–119, 2000.

[68] K. M. Choi and J. A. Rogers, "A photocurable poly(dimethylsiloxane) chemistry designed for soft lithographic molding and printing in the nanometer regime," *Journal of the American Chemical Society*, vol. 125, no. 14, pp. 4060–4061, 2003.

[69] J. N. Lee, C. Park, and G. M. Whitesides, "Solvent compatibility of poly(dimethylsiloxane)-based microfluidic devices," *Analytical Chemistry*, vol. 75.23, pp. 6544–6554, 2003.

[70] S. Sun, Y. Huang, and B. Zhao, "Formation of silica colloidal crystals on soft hydrophobic vs rigid hydrophilic surfaces," *Colloids and Surfaces A: Physicochemical and Engineering Aspects*, vol. 467, pp. 180–187, 2015.

[71] W. Liu, Y. Shen, G. Xiao, X. She, J. Wang, and C. Jin, "Mechanically tunable sub-10 nm metal gap by stretching PDMS substrate," *Nanotechnology*, vol. 28, p. 075301, 2017.

[72] D. Bodas and C. Khan Malek, "Formation of more stable hydrophilic surfaces of PDMS by plasma and chemical treatments," *Microelectronic Engineering*, vol. 83, no. 4, pp. 1277–1279, 2006.

[73] M. Retsch, Z. Zhou, S. Rivera, M. Kappl, X. S. Zhao, U. Jonas, and Q. Li, "Fabrication of large-area, transferable colloidal monolayers utilizing self-assembly at the air/water interface," *Macromolecular Chemistry and Physics*, vol. 210, no. 3-4, pp. 230–241, 2009.

[74] Z. Hórvölgyi, S. Németh, and J. H. Fendler, "Monoparticulate layers of silanized glass spheres at the water-air interface: Particle-particle and particle-subphase interactions," *Langmuir*, vol. 12, no. 4, pp. 997–1004, 1996.

[75] S. Ebnesajjad, "Surface tension and its measurement," in *Handbook of Adhesives and Surface Preparation*. Elsevier, 2011, pp. 21–30.

[76] Y. F. Liu, R. Zhang, and P. V. Braun, "Mechanical deformation–assisted fabrication of plasmonic nanobowties with broken symmetry and tunable gaps," *Particle & Particle Systems Characterization*, vol. 37, no. 2, p. 1900463, 2020.

[77] M. Yao and J. Fang, "Hydrophilic PEO-PDMS for microfluidic applications," *Journal of Micromechanics and Microengineering*, vol. 22, no. 2, p. 025012, 2012.

[78] J. Rybczynski, U. Ebels, and M. Giersig, "Large-scale, 2D arrays of magnetic nanoparticles," *Colloids and Surfaces A: Physicochemical and Engineering Aspects*, vol. 219, no. 1, pp. 1–6, 2003.

[79] Y. J. Zhang, W. Li, and K. J. Chen, "Application of two-dimensional polystyrene arrays in the fabrication of ordered silicon pillars," *Journal of Alloys and Compounds*, vol. 450, no. 1, pp. 512–516, 2008.

[80] S. J. Barcelo, S. T. Lam, G. A. Gibson, X. Sheng, and D. Henze, "Nanosphere lithography based technique for fabrication of large area well ordered metal particle arrays," in *SPIE Advanced Lithography*. International Society for Optics and Photonics, 2012, p. 83232L.

[81] C. Saenz, "Procedure for silanization of su-8/silicon master," Oct. 2015, Microfluidics/Microfabrication Facility Harvard Medical School. [Online]. Available: https://hms.harvard.edu/sites/default/files/Departments/MicrofluidicsandMicrofabricationFacility/files/SilanizationofPhotoresistMasterProtocol.pdf

[82] M. Kim, B. U. Moon, and C. H. Hidrovo, "Enhancement of the thermo-mechanical properties of PDMS molds for the hot embossing of PMMA microfluidic devices," *Journal of Micromechanics and Microengineering*, vol. 23, no. 9, p. 095024, 2013.

[83] Z. Dai, Y. Li, G. Duan, L. Jia, and W. Cai, "Phase diagram, design of monolayer binary colloidal crystals, and their fabrication based on ethanol-assisted self-assembly at the air/water interface," *ACS Nano*, vol. 6, no. 8, pp. 6706–6716, 2012.

[84] X. Fang, C. Zheng, Z. Yin, Z. Wang, J. Wang, J. Liu, D. Luo, and Y. J. Liu, "Hierarchically ordered silicon metastructures from improved self-assembly-based nanosphere lithography," *ACS Applied Materials & Interfaces*, vol. 12, no. 10, pp. 12 345–12 352, 2020.

[85] A. Maestro, L. J. Bonales, H. Ritacco, R. G. Rubio, and F. Ortega, "Effect of the spreading solvent on the three-phase contact angle of microparticles attached at fluid interfaces," *Physical Chemistry Chemical Physics*, vol. 12, no. 42, pp. 14 115–14 120, 2010.

[86] M. Szekeres, O. Kamalin, R. A. Schoonheydt, K. Wostyn, K. Clays, A. Persoons, and I. Dékány, "Ordering and optical properties of monolayers and multilayers of silica spheres deposited by the Langmuir–Blodgett method," *Journal of Materials Chemistry*, vol. 12, no. 11, pp. 3268–3274, 2002.

[87] C. C. Ho, P. Y. Chen, K. H. Lin, W.-T. Juan, and W. L. Lee, "Fabrication of monolayer of polymer/nanospheres hybrid at a water-air interface," *ACS Applied Materials & Interfaces*, vol. 3, no. 2, pp. 204–208, 2011.

[88] R. N. Shimizu and N. R. Demarquette, "Evaluation of surface energy of solid polymers using different models," *Journal of Applied Polymer Science*, vol. 76.12, pp. 1831–1845, 2000.

[89] B. P. Binks, P. D. Fletcher, M. A. Thompson, and R. P. Elliott, "Influence of propylene glycol on aqueous silica dispersions and particle-stabilized emulsions," *Langmuir*, vol. 29.19, pp. 5723–5733, 2013.

[90] B. P. Binks, P. D. Fletcher, M. A. Thompson, and R. P. Elliott, "Effect of added diols (glycols) on the emulsion properties of oil, water and surfactant mixtures," *Colloids and Surfaces A: Physicochemical and Engineering Aspects*, vol. 390.1-3, pp. 67–73, 2011.

[91] K. Gracie, D. Turner, and R. Palepu, "Thermodynamic properties of micellization of sodium dodecyl sulfate in binary mixtures of ethylene glycol with water," *Canadian Journal of Chemistry*, vol. 74.9, pp. 1616–1625, 1996.

[92] M. Gudelj, P. Šurina, L. Jurko, A. Prkić, and P. Bošković, "The additive influence of propane-1, 2-diol on SDS micellar structure and properties," *Molecules*, vol. 26.12, p. 3773, 2021.

[93] M. Bekeris, T. Truong, S. Carron, Z. Karimi, H. Feng, U. Nze, M. Beeman, R. D. Sochol, and R. Warren, "Rapid quantification of nanosphere lithography packing defects using scanning electron microscopy edge effects," *Physica Status Solidi (RRL)–Rapid Research Letters*, vol. 14, no. 11, p. 2000328, 2020.

[94] R. Rengarajan, D. Mittleman, C. Rich, and V. Colvin, "Effect of disorder on the optical properties of colloidal crystals," *Physical Review E*, vol. 71, no. 1, p. 016615, 2005.

[95] V. Canalejas-Tejero, M. Ibisate, D. Golmayo, A. Blanco, and C. López, "Qualitative and quantitative analysis of crystallographic defects present in 2D colloidal sphere arrays," *Langmuir*, vol. 28, no. 1, pp. 161–167, 2012.

[96] A. T. Gray, E. Mould, C. P. Royall, and I. Williams, "Structural characterisation of polycrystalline colloidal monolayers in the presence of aspherical impurities," *Journal of Physics: Condensed Matter*, vol. 27, no. 19, p. 194108, 2015.

[97] Y. K. Koh and C. C. Wong, "In situ monitoring of structural changes during colloidal self-assembly," *Langmuir*, vol. 22, no. 3, pp. 897–900, 2006.

[98] M. Gilbert, "Relation of structure to chemical properties," in *Brydson's Plastics Materials*. Elsevier, 2017, pp. 75–102.

[99] J. Sun, C. jun Tang, P. Zhan, Z. lv Han, Z. S. Cao, and Z. L. Wang, "Fabrication of centimeter-sized single-domain two-dimensional colloidal crystals in a wedge-shaped cell under capillary forces," *Langmuir*, vol. 26.11, pp. 7859–7864, 2010.

[100] F. Bayat, P. Chaghamirzaei, A. Nikniazi, S. A. Kandjani, M. Rashidi, and H. Tajalli, "Optimizing the concentration of colloidal suspensions in convective assembly of centimeter-sized uniform monolayer colloidal crystals," *Applied Surface Science*, vol. 434, pp. 898–904, 2018.

[101] J. Rieger, "The glass transition temperature of polystyrene: Results of a round robin test," *Journal of Thermal Analysis and Calorimetry*, vol. 46, no. 3-4, pp. 965–972, 1996.

[102] K. Xu, R. Zhou, K. Takei, and M. Hong, "Toward flexible surface-enhanced Raman scattering (SERS) sensors for point-of-care diagnostics," *Advanced Science*, vol. 6.16, p. 1900925, 2019.

[103] S. E. Bell, G. Charron, E. Cortés, J. Kneipp, M. L. de la Chapelle, J. Langer, M. Procházka, V. Tran, and S. Schlücker, "Towards reliable and quantitative surface-enhanced Raman scattering (SERS): From key parameters to good analytical practice," *Angewandte Chemie International Edition*, vol. 59.14, pp. 5454–5462, 2020.

[104] S. Almohammed, B. J. Rodriguez, and J. H. Rice, "Nucleobase sensing using highly-sensitive surface-enhanced Raman spectroscopy templates comprising organic semiconductor peptide nanotubes and metal nanoparticles," *Sensing and Bio-Sensing Research*, vol. 24, p. 100287, 2019.

[105] B. Giese and D. McNaughton, "Surface-enhanced Raman spectroscopic and density functional theory study of adenine adsorption to silver surfaces," *The Journal of Physical Chemistry B*, vol. 106, no. 1, pp. 101–112, 2002.

[106] C. Otto, T. J. J. V. den Tweel, F. F. M. D. Mul, and J. Greve, "Surface-enhanced Raman spectroscopy of DNA bases," *Journal of Raman Spectroscopy*, vol. 17.3, pp. 289–298, 1986.

[107] F. Madzharova, Z. Heiner, M. Guhlke, and J. Kneipp, "Surface-enhanced hyper-Raman spectra of adenine, guanine, cytosine, thymine, and uracil," *The Journal of Physical Chemistry C*, vol. 120.28, pp. 15 415–15 423, 2016.

[108] L. E. Hennemann, A. Kolloch, A. Kern, J. Mihaljevic, J. Boneberg, P. Leiderer, A. J. Meixner, and D. Zhang, "Assessing the plasmonics of gold nano-triangles with higher order laser modes," *Beilstein Journal of Nanotechnology*, vol. 3.1, pp. 674–683, 2012.

[109] M. Pagliai, S. Caporali, M. Muniz-Miranda, G. Pratesi, and V. Schettino, "SERS, XPS, and DFT study of adenine adsorption on silver and gold surfaces," *The Journal of Physical Chemistry Letters*, vol. 3, no. 2, pp. 242–245, 2012.

[110] S. G. Harroun, "The controversial orientation of adenine on gold and silver," *ChemPhysChem*, vol. 19.9, pp. 1003–1015, 2018.

[111] P. G. Spizzirri, J. H. Fang, S. Rubanov, E. Gauja, and S. Prawer., "Nano-Raman spectroscopy of silicon surfaces," *arXiv Preprint*, vol. arXiv:1002.2692, 2010.

[112] C. L. Haynes and R. P. Van Duyne, "Plasmon-sampled surface-enhanced Raman excitation spectroscopy," *The Journal of Physical Chemistry B*, vol. 107.30, pp. 7426–7433, 2003.

[113] V. Sivaprakasam and M. B. Hart, "Surface-enhanced Raman spectroscopy for environmental monitoring of aerosols," *ACS Omega*, vol. 6.15, pp. 10 150–10 159, 2021.

[114] D. E. Wolf, "What is the confocal volume?" [Online]. Available: http://www.fcsxpert.com/classroom/theory/pdfs/fcs_confocal.pdf

[115] C. Kim, S. Baek, Y. Ryu, Y. Kim, D. Shin, C. W. Lee, W. Park, A. M. Urbas, G. Kang, and K. Kim, "Large-scale nanoporous metal-coated silica aerogels for high SERS effect improvement," *Scientific Reports*, vol. 8.1, pp. 1–10, 2018.

[116] N. J. Everall, "Confocal Raman microscopy: Performance, pitfalls, and best practice." *Applied Spectroscopy*, vol. 63.9, pp. 245A–262A, 2009.

[117] J. E. Freund, M. Edelwirth, P. Kröbel, and W. M. Heckl., "Structure determination of two-dimensional adenine crystals on graphite," *Physical Review B*, vol. 55.8, p. 5394, 1997.

[118] R. G. Acres, X. Cheng, K. Beranová, S. Bercha, T. Skála, V. Matolín, Y. Xu, K. C. Prince, and N. Tsud, "An experimental and theoretical study of adenine adsorption on Au (111)," *Physical Chemistry Chemical Physics*, vol. 20.7, pp. 4688–4698, 2018.

[119] J. Wang, J. Li, C. Zeng, Q. Qu, M. Wang, W. Qi, R. Su, and Z. He, "Sandwich-like sensor for the highly specific and reproducible detection of rhodamine 6G on a surface-enhanced Raman scattering platform," *ACS Applied Materials & Interfaces*, vol. 12, no. 4, pp. 4699–4706, 2020.

[120] Y. C. Chen and H. Yang, "Octopus-inspired assembly of nanosucker arrays for dry/wet adhesion," *ACS Nano*, vol. 11, no. 6, pp. 5332–5338, 2017.

[121] F. S. Ameer, C. U. Pittman Jr, and D. Zhang, "Quantification of resonance Raman enhancement factors for rhodamine 6G (R6G) in water and on gold and silver nanoparticles: Implications for single-molecule R6G SERS," *The Journal of Physical Chemistry C*, vol. 117, no. 51, pp. 27 096–27 104, 2013.

[122] Pérez-Jiménez, A. Isabel, D. Lyu, Z. Lu, G. Liu, and B. Ren, "Surface-enhanced Raman spectroscopy: Benefits, trade-offs and future developments," *Chemical Science*, vol. 11.18, pp. 4563–4577, 2020.

[123] L. Jensen and G. C. Schatz, "Resonance Raman scattering of rhodamine 6G as calculated using time-dependent density functional theory," *The Journal of Physical Chemistry A*, vol. 110.18, pp. 5973–5977, 2006.

[124] M. Kahraman, E. R. Mullen, A. Korkmaz, and S. Wachsmann Hogiu, "Fundamentals and applications of SERS-based bioanalytical sensing," *Nanophotonics*, vol. 6, no. 5, pp. 831–852, 2017.

[125] D. Kim, A. R. Campos, A. Datt, Z. Gao, M. Rycenga, N. D. Burrows, N. G. Greeneltch, C. A. Mirkin, C. J. Murphy, R. P. Van Duyne, and C. L. Haynes, "Microfluidic-SERS devices for one shot limit-of-detection," *Analyst*, vol. 139, no. 13, pp. 3227–3234, 2014.

[126] F. Laible, D. A. Gollmer, S. Dickreuter, D. P. Kern, and M. Fleischer, "Continuous reversible tuning of the gap size and plasmonic coupling of bowtie nanoantennas on flexible substrates," *Nanoscale*, vol. 10, no. 31, pp. 14 915–14 922, 2018.

[127] J. Merlein, M. Kahl, A. Zuschlag, A. Sell, A. Halm, J. Boneberg, P. Leiderer, A. Leitenstorfer, and R. Bratschitsch, "Nanomechanical control of an optical antenna," *Nature Photonics*, vol. 2, no. 4, pp. 230–233, 2008.

[128] W. Liu, Q. Zou, C. Zheng, and C. Jin, "Metal-assisted transfer strategy for construction of 2d and 3d nanostructures on an elastic substrate," *ACS Nano*, vol. 13, no. 1, pp. 440–448, 2018.

[129] "Adenine(a8626) product information." [Online]. Available: https://www.sigmaaldrich.com/deepweb/assets/sigmaaldrich/product/documents/119/460/a8626pis.pdf

[130] H. H. Jeong, M. C. Adams, J. P. Gunther, M. Alarcon-Correa, I. Kim, E. Choi, C. Miksch, A. F. Mark, A. G. Mark, and P. Fischer, "Arrays of plasmonic nanoparticle dimers with defined nanogap spacers," *ACS Nano*, vol. 13, no. 10, pp. 11 453–11 459, 2019.

[131] V. Flauraud, R. Regmi, P. M. Winkler, D. T. Alexander, H. Rigneault, N. F. Van Hulst, M. F. Garcia-Parajo, J. Wenger, and J. Brugger, "In-plane plasmonic antenna arrays with surface nanogaps for giant fluorescence enhancement," *Nano Letters*, vol. 17, no. 3, pp. 1703–1710, 2017.

[132] Z. Jiang and J. H. Pikul, "Centimetre-scale crack-free self-assembly for ultra-high tensile strength metallic nanolattices," *Nature Materials*, pp. 1–7, 2021.

[133] C. M. Hsu, S. T. Connor, M. X. Tang, and Y. Cui, "Wafer-scale silicon nanopillars and nanocones by Langmuir-Blodgett assembly and etching," *Applied Physics Letters*, vol. 93, no. 13, p. 133109, 2008.

[134] D. Ji, T. Li, and H. Fuchs, "Nanosphere lithography for sub-10-nm nanogap electrodes," *Advanced Electronic Materials*, vol. 3, no. 1, p. 1600348, 2017.

[135] J. Mertens, A. L. Eiden, D. O. Sigle, F. Huang, A. Lombardo, Z. Sun, R. S. Sundaram, A. Colli, C. Tserkezis, J. Aizpurua, A. C. Ferrari, and J. J. Baumberg, "Controlling subnanometer gaps in plasmonic dimers using graphene," *Nano Letters*, vol. 13, no. 11, pp. 5033–5038, 2013.